SAPIENZA
UNIVERSITÀ DI ROMA

Gold nanoparticles labelled with an alpha emitter: a theragnostic double therapy agent for Non-Hodgkin Lymphoma and Paragranuloma

Department of General, Specialist Surgery and Anesthesiology "Paride Stefanini"

PhD in "Advances in Cardio-Thoracic and Vascular Pathophysiology and Imaging" 38th cycle

Dr. Miriam Conte
1545312

Supervisor
Prof. Giuseppe De Vincentis

Co-Supervisor
Prof. Viviana Frantellizzi

A.Y. 2024/2025

Alla mia famiglia.
A chi mi ha insegnato il valore della presenza reale restandomi accanto nei momenti bui.
A chi mi ha ricordato che la prima presenza da augurarsi è quella che si sa donare a sé stessi.
Al mio idealismo, pagato a peso d'oro, che ha dato un paio di gambe ai miei sogni affinché camminassero lungo il sentiero della vita.

Table of Contents

Abstract

Background: The use of gold nanoparticles (AuNPs) in theranostics represents a thrilling and novel perspective for oncology. AuNPs can induce cell death through the so-called "plasmonic photothermal therapy" (or PTT). It consists of the conversion of the incident laser beam light into heat, inducing cell death. In this study, double-layer keratin gold bipyramid nanoparticles (DL-Ker-AuBPys), single-layer keratin gold bipyramid nanoparticles (SL-Ker-AuBPys), and gold nanorods (AuNRs) were evaluated in terms of toxicity, biocompatibility, and were labelled with Radium-223 ($^{223}RaCl_2$, radium). Gelatine-Na_2HPO_4 and DTPA were evaluated as possible chelating agents able to improve radiolabelling with radium. The functionalization with the mouse monoclonal antibody 1011:sc-57709 was then explored to obtain target-specific nanoparticles. This work aimed to develop a potential theragnostic agent useful to achieve therapeutic radicality in Non-Hodgkin lymphoma (NHL) and nodular lymphocyte-dominant Hodgkin lymphoma (NLPHL) in association with radio-chemotherapy. This could be realized by combining the therapeutic features of $^{223}RaCl_2$ and AuNPs with the gamma emission of $^{223}RaCl_2$.

Methods: Stable colloidal AuBPs were prepared through a seed-mediated growth approach and were functionalized with keratin. U87-MG cells were used to evaluate the biocompatibility of AuBPs through a trypan blue exclusion assay. After the incubation with AuBPs, the evaluation of U87-MG cell viability was determined through laser illumination: U87-MG cells (5×10^5) were incubated for 24 and 48 h with 100 μM DL- Ker-AuBPs and were illuminated for 6 minutes. In the second part of the work, DL-Ker-AuBPs were incubated with 0.25 ml of $^{223}RaCl_2$ (activity of 0.9 MBq in 1.6 ml) for 5, 15, and 30 minutes at room temperature. Then, a total quantity of 0.5 ml DL-Ker-AuBPys was placed vertically in a shielded water bath at 45°C, 0.25 ml of $^{223}RaCl_2$ was added, and samples were taken at 0, 5, 15, and 30 minutes and after 20 minutes of cooling at room temperature. Instant thin-layer chromatography (ITLC) was conducted for strips with DL-Ker-AuBPys, $^{223}RaCl_2$-DL-Ker-AuBPys, and $^{223}RaCl_2$ alone. A Perkin Elmer Lambda 365 spectrophotometer was used to acquire reflectance and absorption spectra of strips and of DL-Ker-AuBPys and $^{223}RaCl_2$-DL-Ker-AuBPys solutions to study if an effective radiolabelling had occurred. The strips were examined by a thermal scan with an 808 nm light beam to establish the precise localization of the nanoparticles. The pH value of $^{223}RaCl_2$-DL-Ker-AuBPys solution was measured after 30 minutes of incubation at room temperature and post-cooling after 30 minutes of incubation at 45°C. To better the labelling with $^{223}RaCl_2$, gelatine-Na_2HPO_4 and diethylenetriaminepentaacetate (DTPA) were evaluated as chelating agents: absorbance spectra were acquired for $^{223}RaCl_2$-DTPA-NRs and $^{223}RaCl_2$-gelatine-Na_2HPO_4-AuNRs solution to demonstrate the functionalization of gold nanocarrier with the chelating agent. ITLC was performed only for $^{223}RaCl_2$-DTPA-NRs. In the last year of the study, AuNRs were functionalized with PAH (polycyclic aromatic hydrocarbons) and bioconjugated with mouse monoclonal antibodies 1011:sc-57709. Absorbance spectra of AuNRs and AuNRs/PAH/Ab solution were performed to determine the effective functionalization of AuNRs.

Results: DL-Ker-AuBPys demonstrated a high degree of biocompatibility. Conversely, SL-Ker-AuBPys were toxic for U87-MG cells starting from a concentration of 50 μM at 24h and 10 μM at 48 and 72h. DL-Ker-AuBPys greatly induce cell death in U87-MG cells when they are not washed out before the illumination. The labelling yield of 5 minutes of incubation of $^{223}RaCl_2$ with DL-Ker-AuBPys at room temperature was 7.8%. No significant changes in the labelling yield or in the pH value (equal to 6) were found when incubation time and temperature were modified. However, the reflectance spectra of the strips dipped in saline, respectively with $^{223}RaCl_2$-DL-Ker-AuBPs and DL-Ker-AuBPs, suggested effective radiolabelling. It was also confirmed by the absorption spectrum of $^{223}RaCl_2$-DL-Ker-AuBPs solution. Thermal scanning of the strips with $^{223}RaCl_2$-DL-Ker-AuBPs and DL-Ker-AuBPs showed localized heating around the center where the drop was deposited, confirming the presence of NPs. DL-Ker-AuBPs demonstrated high viability when incubated for 24 and 48 hours with U87-MG cells. Gelatine-Na_2HPO_4 was shown to be a possible candidate as a chelator agent, but only decayed $^{223}RaCl_2$ was used for this functionalization experiment. DTPA betters the labelling of AuNRs, demonstrating to be an excellent chelating agent for the radiolabelling of AuNRs. Finally, the use of PAH permitted the functionalization of AuNRs with antibodies, creating a novel theragnostic tool feasible for the treatment of LNH and NLPHL micrometastases.

Conclusions: DL-Ker-AuBPs are biocompatible nanocarriers with great photothermal capacity to induce cellular death. They were successfully labelled with $^{223}RaCl_2$, but with low label efficiency, which is not improved by modifying incubation time and temperature. AuNRs have been demonstrated to be a better candidate for theragnostics thanks to their easier labelling and functionalization with antibodies. However, further studies are required to better evaluate the feasibility of use in clinical trials.

1. Introduction

A novel nuclear medicine approach in the oncological field employs radiopharmaceuticals both in diagnostics and therapy, in the so-called *theragnostics*. The capability of some isotopes to emit gamma rays or positrons and alpha or beta particles permits obtaining diagnostic information and therapeutic effects.

The advent of nanomedicine revolutionized the approach in oncology and realized the most diverse biomedical applications that span from diagnostics, sensing, and cellular imaging to drug delivery and prevention using nanostructures. The possibility of combining therapy and diagnosis is achieved by the advent of *nanotheranostics*, a branch of medicine that integrates nanotechnology to enable multi-level diagnostic and therapeutic prospects to gain more precision and efficacy.

Another innovative therapeutic approach is the hyperthermia elicited in cancer cells by ferromagnetic materials such as magnetite (-Fe_3O_4), maghemite (-Fe_2O_3), and hematite (-Fe_2O_3) [1] or gold nanoparticles (AuNPs) arranged in various structures, graphene, carbon nanotubes (CNTs), semiconductor quantum dots (QDs) that exhibit optical absorbance in the near infrared region (NIR) [2]. AuNPs, but also graphene and carbon, thanks to their optical properties, can be used to achieve the death of cancer cells through photothermal therapy (photothermal therapy, PTT). The rationale of PTT is to deliver the nanocarrier toward a specific molecular target of a cancer cell and then hit the nanocarrier with a specific laser beam in the NIR. Thanks to the phenomenon known as *localized plasmonic resonance* (LPR), when the laser hits NPs, the external electrons of the nanocarrier surface excite and release heat, causing cancer cell death through heat damage [3]. This phenomenon is due to the localized collective excitation of conduction electrons on the surface of AuNPs, which produce strong absorption plasmon bands (plasmons). Plasmon locations vary widely across the electromagnetic spectrum, ranging from the visible to the near-infrared (NIR) area, contingent upon the size, shape, and surrounding refractive index of the AuNPs [4]. In particular, the possibility of modulating the laser power and the volume of AuNPs modifies the thermal ablation characteristic length of the gold NPs, which is the spatial extension of temperature above the ablation threshold around the NPs [5]. So, it is reliable to be effective, sparing as much normal tissue as possible. To confine the heat produced by nanoparticle activation, it is important to keep the LPR of the NPs near the first (700-900 nm) or second (1000-1300 nm) biological window, where tissue absorption is low and radiation penetration depth is high. Therefore, NIR laser (≈800 nm) is preferable to achieve better tissue penetration. In fact, NIR has a high propagation (more than 3 mm), while green light is absorbed and transformed into heat energy [6].

The opportunity to radiolabel a nanocarrier with an alpha emitter represents a further thrilling field, since, thanks to a tissue penetration corresponding to 28-100 μm (5–10 cell diameters), it allows for restricting the radiation deposition to the target cells and only to the immediate neighbouring cells [7].

This fascinating prospect led our group to evaluate the possibility of labelling AuNPs with $^{223}RaCl_2$ to treat superficial bone metastases or micrometastases, such as metastases in superficial lymph nodes, or in association with surgery to ablate the residual disease, in Non-Hodgkin lymphoma (NHL) and paragranuloma (NLPHL).

1.1 Non-Hodgkin lymphoma and paragranuloma: possible applications for nanomedicine

Non-Hodgkin lymphoma is the most widespread haematological tumour worldwide and includes different classes of lymphoid neoplasms deriving from T and B cells. Unlike Hodgkin lymphoma (HL), it is characterized by the absence of the Reed-Sternberg cell and by negativity to histological staining for CD15 and CD30 [8]. 95% of the lymphomas included in this category express the non-glycosylated phosphoprotein CD20, exclusive of mature and immature B lymphocytes membrane surface [9] and absent in plasma [10]. Such a protein behaves like a calcium channel and is involved in cell cycle initiation and cell differentiation. Due to its homogeneity of expression on the cell membrane (with an expression density $>10^5$ per cell), CD20 represents an attractive therapeutic target in NHL [11,12].

A similar feature is shared by another class of lymphoma, the nodular lymphocyte-dominant Hodgkin lymphoma, also known as paragranuloma (NLPHL). It represents 5-16% of all Hodgkin lymphomas [13] and has peculiar characteristics that differentiate it from the classic variant of HL, such as predominance in males and indolent clinical trends [14], a high rate of relapses, and the tendency to transform into diffuse large B-cell lymphoma (DLBCL) variant [15]. It is also characterized by the presence of classic markers of a lymphocyte, such as CD20 positivity and CD15 and CD30 negativity [16–18]. This last characteristic makes NLPHL a valid candidate for anti-CD20 monoclonal antibody therapies.

1.2 Chemical aspects of gold nanoparticles

Gold nanoparticles have a central role in nanomedicine since, as thermo-optical transducers for plasmonic photothermal therapy (PPTT), they represent a huge resource for oncology. A pivotal

aspect to take into account for the clinical application of a nanocarrier is its biocompatibility and stability. In particular, for AuNPs, the aggregation should be avoided since it could induce electromagnetic field enhancement, determining the cellular temperature elevation. This could be avoided if a lower laser power is used to elicit PPTT [5]. Different coating techniques have been explored to overcome these issues. First of all, the use of spherical AuNPs (or nanospheres, NSs) has been explored. However, the common use of CTAB as a stabilizing agent for gold represents an issue because of the known toxicity [19]. It shifted this research to new approaches to stabilize and improve the biocompatibility of nanoparticles. In previous research of Frantellizzi et al. [4], AuNPs were functionalized with keratin, obtaining DTPA-assisted ^{99m}Tc-labelled Ker-AuNPs, which demonstrated to be an excellent biocompatible candidate for PTT application. Given these findings, keratin-AuNPs were taken into consideration for this work.

Firstly, both the NSs and the bipyramid nanoparticles (BPys) were then evaluated. Metallic nanoparticles with an anisotropic shape, such as bipyramids, exhibit two distinct types of surface plasmon absorption peaks as a result of the collective movement of quasi-free electrons along the BPy's longer and shorter axes, known as longitudinal and transverse surface plasmon resonances, respectively [20]. For this reason, BPys have been selected for coating experiments. Single-layer keratin-AuBPys (SL-Ker-AuBPys) and double-layer keratin-AuBPys (DL-Ker-AuBPys) were evaluated regarding biocompatibility and photothermal capacity to induce cellular death. Then, a double layer of keratin was chosen to coat the AuBPys for their excellent biocompatibility and photothermal properties. A novel theragnostic tool conjugating alpha therapy and PTT in one molecule was then proposed: DL-Ker-AuBPys labelled with $^{223}RaCl_2$ ($^{223}RaCl_2$-DL-Ker-AuBPys).

To better the labelling of AuNPs with $^{223}RaCl_2$, thus, the possibility of using gelatine-Na_2HPO_4 as a bridge between gold nanorods (AuNRs) and $^{223}RaCl_2$ was evaluated. The study was conducted through the acquisition of absorbance spectra of the solutions with gelatine-Na_2HPO_4-AuNRs and the same solution radiolabelled with increasing concentrations of decayed $^{223}RaCl_2$, all of them at time zero and after 24 hours. The same line of thought leads to evaluating the feasibility of using Diethylenetriaminepentaacetate (DTPA) as a chelator after AuNRs were heated to 45 °C for 15 min. ITLC studies were then conducted at different times of incubation with $^{223}RaCl_2$.

The possibility of creating a tumour-specific weapon was explored through functionalization experiments of AuNRs with mouse monoclonal antibodies 1011:sc-57709. The functionalization with the antibodies makes the homing to specific targets possible, opening the chance to develop a nanocarrier characterized by a photothermal and alpha particles-mediated therapeutic effect.

2. Materials and methods

2.1 Colloidal gold nanobipyramids (AuBPys) synthesis

Tetrachloroauric acid (HAuCl4•4H2O, 99.99%), cetyltrimethylammonium bromide (CTAB, 96%), nitric acid (HNO3, 65%), citric acid (C6H8O7), cetyltrimethylammonium chloride (CTAC), hydroxyquinoline (HQL, C9H7NO, 99%), sodium borohydride (NaBH4, 99%) and silver nitrate (AgNO3, 99%), were purchased from Sigma-Aldrich. The previously reported seed-mediated growth approach was adapted and employed for the synthesis of stable colloidal AuBPys with high yield [23]. Briefly, the first step relies on the preparation of the Au seeds by mixing under mild stirring conditions 25 mM $HAuCl_4•4H_2O$, 25 w% CTAC surfactant, 0.25 M HNO_3, 50 mM $NaBH_4$ reducing agent, and 1 M citric acid. The final solution was placed in a water bath for 2 hours at 85 ºC. In the second step of the synthesis process, 19 μl of the as-prepared Au seeds are added to the growth solution consisting of 25 mM $HAuCl_4$, 45 mM CTAB stabilising agent solution, 5 mM $AgNO_3$, and 0.4 M HQL as a reducing agent, the latter being added in a two-step manner. Concretely, 2/3 of the HQL volume was added during the growth solution preparation. The remaining amount was mixed with the final solution during the growth of the AuBPys, specifically after 15 minutes of its thermal treatment. The growth solution was further thermally treated for 35 minutes at 45ºC. To remove any reactant excess, the synthesised AuBPys underwent 1 purification step through centrifugation at 8000 RPM for 15 minutes and redispersion of the precipitate in ultrapure water (resistivity ~ 18.2 MΩ).

2.2 Synthesis of DL-Ker-AuBPys

Sodium citrate was used as a reducing agent in the Turkevich technique [24] to create AuNPs. DLS measurements have shown that the resulting naked AuNPs have a spherical form with an average diameter of around 30 nm[25]. To achieve a 1:100 weight ratio between Au and keratin, 1.5 mM solutions of Ker-AuNPs and AuNPs were combined with the keratin solution. The total quantity of keratin used was three orders of magnitude, so all the AuNPs' binding sites were saturated. Following an overnight stir, two centrifugations at 14,300 RPM to eliminate any remaining free keratin, and a final resuspension in MilliQ water, the resulting Ker-AuNPs solution was obtained. The presence of keratin surrounding AuNPs has previously been shown using X-ray

photoelectron spectroscopy (XPS) and Fourier Transformed Infrared Spectroscopy (FTIR) studies [25].

2.3 Cell cultures

U87-MG cell line was purchased from CLS (Cell Lines Service GmbH, Eppelheim, Germany) and cultured as already reported by Rosa et al. [21]. U87-MG cells were grown in Dulbecco's Modified Eagle Medium (DMEM) supplemented with 10% heat-inactivated Fetal Bovine Serum (FBS, Sigma-Aldrich, St. Louis, MO), 100 IU/ml penicillin G, 100 µg/ml streptomycin, 1% L-glutamine, 1% nonessential amino acids, and 1mM sodium pyruvate in a cell incubator with humidified atmosphere and controlled parameters of temperature (37°C) and CO_2 percentage (5%). The medium was replaced twice a week, and cells were subcultured only when 85% confluence was reached.

2.4 Ker-AuBPys toxicity evaluation

The evaluation of Ker-AuBPys toxicity was assessed by trypan blue exclusion assay following the protocol already reported by Scibetta et al. [22]. U87-MG cells (5 x 105) were incubated with different concentrations (0-100 µM) of either single-layer or double-layer Ker-AuBPys for different times (0-72 h). At the end of each experiment, cells were harvested, incorporated with trypan blue, and automatically counted by the Countess Cell Counter (Thermo Fisher Scientific, Waltham, MA, USA). Three independent experiments were performed in triplicate, and the results were expressed as mean ± SD.

2.5 Viability study after illumination of DL-Ker-AuBPys

U87-MG cells were used to prove cellular viability. After an incubation of 24h and 48h with 100 µM DL-Ker-AuBPys, the cells were illuminated with a laser for 6 minutes after washing and without washing the excess of nanoparticles. After this time, cells were harvested, incorporated with trypan blue and automatically counted by the Countess Cell Counter (Thermo Fisher Scientific, Waltham, MA, USA). Three independent experiments were performed in triplicate, and results were expressed as mean ± SD.

2.6 Radiolabelling of DL-Ker-AuBPys with $^{223}RaCl_2$

0.5 ml of DL-Ker-AuBPys solution and 0.25 ml of $^{223}RaCl_2$ (activity of 0.9 MBq in 1.6 ml) were incubated for 5, 15, and 30 minutes at room temperature. A total quantity of

0.5ml DL-Ker-AuBPys was placed vertically in a shielded water bath at 45°C, and 0.25 ml of $^{223}RaCl_2$ was added. Samples were taken at 0, 5, 15, and 30 minutes and after 20 minutes of cooling at room temperature.

2.7 Evaluation of pH value of the $^{223}RaCl_2$-DL-Ker-AuBPys solution

The pH value of the $^{223}RaCl_2$-DL-Ker-AuBPys solution was measured after 30 minutes of incubation at room temperature and after 30 minutes of incubation at 45°C post cooling.

2.8 *Single-photon emission computed tomography (SPECT) imaging*

A gamma camera equipped with low-energy high-resolution (LEHR) collimators (Millennium, GE Healthcare, USA) outfitted with 59 circular PMTs (76 mm and 38 mm), a NaI(Tl) scintillation crystal (thickness ¼ 9.5 mm), a NEMA UFOV 40 x 60 cm, and an energy range of 40–511 keV was used to perform SPECT imaging studies. Images of the tube with DL-Ker-AuBPys labelled with $^{223}RaCl_2$ incubated at room temperature for 5 minutes were acquired with 1.5 zooms, 512 x 512 spatial resolution, and a 10-minute acquisition period. The dimensions of one pixel are 1.2 x 0.8 mm.

2.9 Radiolabelling of DTPA-AuNRs with $^{223}RaCl_2$

A quantity of 0.5 ml of AuNRs was heated to 45 °C for 15 min. Then, 1 ml of DTPA was added to the AuNRs solution and, thus, incubated for 15 min.
After, 1 ml of Radium-223 was added and incubated for 10, 20, and 30 minutes.

2.10 Radiochemical purity (RCP) evaluation of $^{223}RaCl_2$-DL-Ker-AuBPys and $^{223}RaCl_2$-DTPA-AuNRs via ITLC

Instant thin-layer chromatography (ITLC) tests were performed to separate the amounts of $^{223}RaCl_2$-DL-Ker-AuBPys and $^{223}RaCl_2$-DTPA-AuNRs from the unlabelled DL-Ker-AuBPys and DTPA-AuNRs, respectively, and to assess label efficiency. Whatman strips 1 (20x2.5 cm) were used for migration in physiological and ITLC-SG strips (20x2 cm) for migration in methylethylketone (MEK). The ITLC was conducted for radiolabelled AuBPys and AuNRs and for $^{223}RaCl_2$. Each ITLC strip had a drop of $^{223}RaCl_2$-DL-Ker-AuBPys or $^{223}RaCl_2$-DTPA-AuNRs solution (about 5 µl) or $^{223}RaCl_2$ alone placed at the

previously designated beginning position 2 cm from the inferior edge (*pale*). The prepared ITLC strips were inserted vertically into each Falcon tube filled with solvent to a depth of 2 cm from the bottom, with the deposition point kept toward the bottom. After that, the chambers remained closed. Two mobile phases were used: NaCl and MEK to submerge each strip. The activity of the used $^{223}RaCl_2$ sample was 1 MBq in 1 ml. To obtain homogeneous drops (5 μL per drop), 27 Gx1/2 needles were used (0.4mmx13mm). It took the strips 30 minutes for NaCl and 6 minutes for MEK to reach the solvent front and finish their development. After the development was finished, a phosphor imaging device (Cyclone Plus, PerkinElmer Analytics) was used to measure the quantity of radioactive chemicals on the strips. For 20 seconds, the strips were brought into proximity to a phosphor screen, allowing the screen to absorb their radioactivity. After that, each strip was put into a rotating mechanism, the Cyclone, and a red laser beam was used to scan it point by point. After the signal was sent to a high-efficiency photomultiplier, a digital processing system produced high-resolution (up to 600 DPI) digital images that contained quantitative data about the distribution of the radioactivity on the strip represented by a graph.

2.11 UV-VIS spectroscopy

A UV-VIS Perkin-Elmer®LAMBDA 365™ spectrophotometer was used to acquire reflectance and absorption spectra of strips with labelled and unlabelled DL-Ker-AuBPys, and for DL-Ker-AuBPys and $^{223}RaCl_2$-DL-Ker-AuBPys solutions.

2.12 Thermo-optical setup

The thermo-optical setup used to irradiate the strips is shown in Fig. 1. A continuous wave (CW) diode laser (Coherent Powerline) operating at 808 nm was used to illuminate the sample in a direction perpendicular to the air/sample interface. Its emission wavelength corresponds to the longitudinal plasmonic absorption band of the DL-Ker-AuBPys. The power density of the laser was set at 908 mW/cm², following preliminary measurements to optimise measurement times. A FLIR (A655sc) thermal-camera (FLIR System, Wilsonville, OR, USA) equipped with a close-up IR objective was used to measure the temperature variations at the air/sample interface. The thermal camera was connected to a computer equipped with the Research-IR software, which was used to study the variation of the average surface temperature of the sample in the time domain. To assess the mean temperature values achieved in the sample volume, a square region of interest (ROI)

corresponding to the lit area was picked on thermographic images. The illumination protocol chosen was: 5 seconds laser off, 2 minutes laser on and 1 minute laser off.

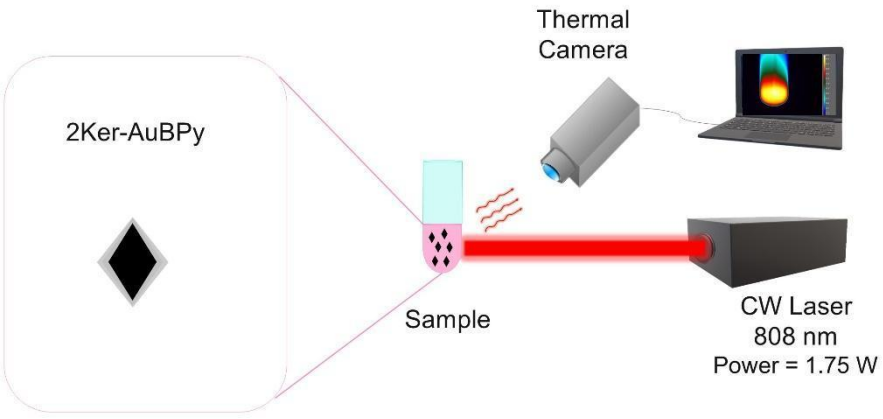

Fig.1: The figure represents a scheme of the thermo-optical setup used to characterize the samples.

2.13 Gelatine solution production

A solution of 100 ml milliQ was used to dissolve 100 mg of gelatine, obtaining a solution of 1 mg/ml concentration.

2.14 Synthesis of gelatine-AuNRs

The solutions of 10 mg/ml EDC and NHSS were obtained by adding 1 ml of milliQ to 10 mg of EDC and 6.2 mg of NHSS to 0.62 ml of milliQ, respectively. The solution of gold nanords (AuNRs) was prepared by mixing 150 ml of milliQ to 16 ml of AuNRs precipitate solution. The crosslinking reaction between gelatine and AuNRs was realized adding 10 µL of EDC and 20 µL of NHSS to the solution of AuNRs. The final solution was transferred to a 4 ml vial and magnetically stirred for 15 minutes. The solution was placed in a 1.5 ml Eppendorf and centrifuged for 10 minutes at 10,000 RPM with an IKA C-MAG HS7 centrifuge. The supernatant was then removed. 500 µL of milliQ and 7 µL of gelatine solution were added to the precipitated AuNRs. Afterwards, the solution was left in magnetic agitation for 1 hour to produce the gelatine-AuNRs solution.

2.15 Radiolabelling of gelatine-AuNRs with decayed $^{223}RaCl_2$

A vial of 6 mL Radium-223 dichloride ($^{223}RaCl_2$, Xofigo®, Bayer) was used for the radiolabelling of gelatine-AuNRs. Each ml of $^{223}RaCl_2$ solution contained 0.58 ng of radium-223 with a pH between 6 and 8. The vial was dated September 2022, so only stable Lead-207 (^{207}Pb) was presumably contained in the vial.

10 µL of Na_2HPO_4 in milliQ solution (120 mM) was added to the gelatine-AuNRs solution and magnetically stirred for 5 minutes. Then, 20 µL of decayed $^{223}RaCl_2$ was added and the final solution was magnetically stirred for another 15 minutes. A quantity of 20 µL of decayed $^{223}RaCl_2$ was consecutively added another 11 times. As the final step, 20 µL of decayed $^{223}RaCl_2$ (for a total of 517 µL) was then added.

2.16 Absorbance spectra of AuNRs, gelatine-AuNRs, and $^{223}RaCl_2$-gelatine- Na_2HPO_4 -AuNRs solution

The absorbance spectroscopy was performed for AuNRs solution, gelatine-AuNRs and $^{223}RaCl_2$-gelatine- Na_2HPO_4 -AuNRs solutions with a Perkin Elmer UV/VIS Lambda 365 spectrophotometer using a quartz crystal cuvette. The blank control was performed by filling the cuvette with 200 µL of milliQ, while 200 µL of AuNRs solution and gelatine-AuNRs solution were consecutively added to the cuvette to obtain each absorbance spectra. The absorbance spectrum was acquired only for the solutions with 20, 40, 60, 120, 140, 200, 240, and 517 µL of decayed $^{223}RaCl_2$. After 24 hours, other absorbance measurements were conducted for the gelatine-AuNRs solution and for the gelatine-Na_2HPO_4-AuNRs with 517 µL of decayed $^{223}RaCl_2$, both prepared the day before.

2.17 Functionalization of AuNRs with antibodies

AuNRs were functionalized with PAH and bioconjugated with antibodies. Commercial dispersions of pristine AuNRs were concentrated four times. A predetermined volume of PAH stock solution (10 mg mL^{-1} prepared in 10 mM NaCl solution, pH 2) and 50 µL of 10 mM NaCl were added to the AuNRs solution. The solution was then maintained for 30 minutes under magnetic stirring. The excess PAH was removed by centrifugation at 14 000 rpm for 8 min at 4 °C, and the pellet was redispersed in 1.2 mL of deionised water. To

initiate the electrostatic coupling mediated by the PAH, 60 µL of Ab stock solution (0.1 mg mL^{-1}) was added, and the dispersion was left to incubate for 30 minutes at room temperature with magnetic stirring. The resultant bioconjugate, AuNRs/PAH/Ab, was extracted by centrifugation (14 000 rpm, 15 min, 4 °C). The concentrations of AuNRs/PAH/Ab were adjusted to provide the same optical density of 0.5 absorbance units. The mouse monoclonal antibody 1011:sc-57709 (or Ab) was obtained from Santa Cruz Biotechnology, Inc.

3. Results

3.1 Viability study results

SL-Ker-AuBPy and DL-Ker-AuBPy were successfully synthetized (fig. 1) and were evaluated in terms of toxicity on U87-MG cells. DL-Ker-AuBPy showed a high degree of biocompatibility.

In particular, SL-Ker-AuBPys proved to be toxic for U87-MG cells starting from a concentration of 50 µM at 24h and 10 µM at 48 and 72h (fig 2).

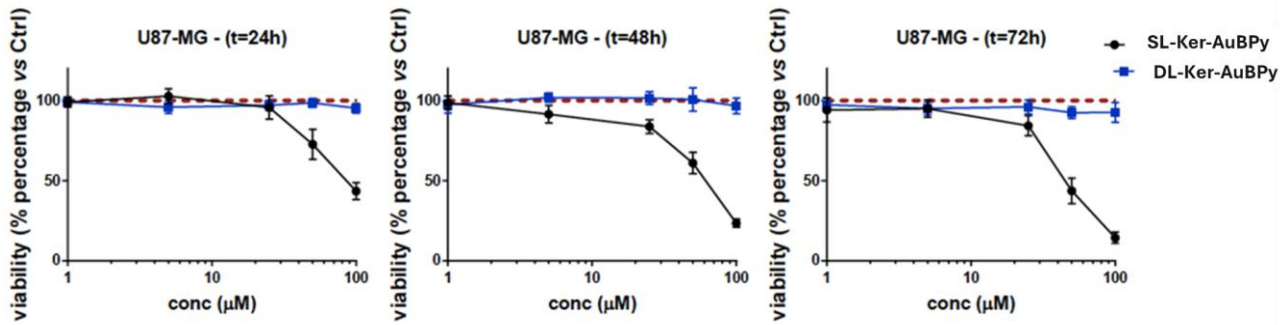

Fig 2: U87-MG incubated respectively with SL-Ker-AuBPy (black dotted line) and DL-Ker-AuBPy (blue dotted line) for 24h, 48h, and 72h. At maximum concentration, the viability of cells incubated with DL-Ker-AuBPy was near 100%.

DL-Ker-AuBPy demonstrated excellent biocompatibility even at 100 µM.

Subsequently, DL-Ker-AuBPys were tested for their photothermal capacity to induce cell death. U87-MG cells were incubated for 24 and 48 h with 100 µM Ker-AuBPys and illuminated for 6 minutes. Their viability was then evaluated. The results clearly showed the great photothermal capacity of DL-Ker-AuBPy that greatly induces cell death in U87-

MG cells when they are not washed out before illumination. Contrarily, when the excess of nanoparticles is removed, they are not able to elevate the intracellular temperature enough to cause cell death, which could be due to a difficulty to penetrate the cell membrane caused by their size (fig. 3).

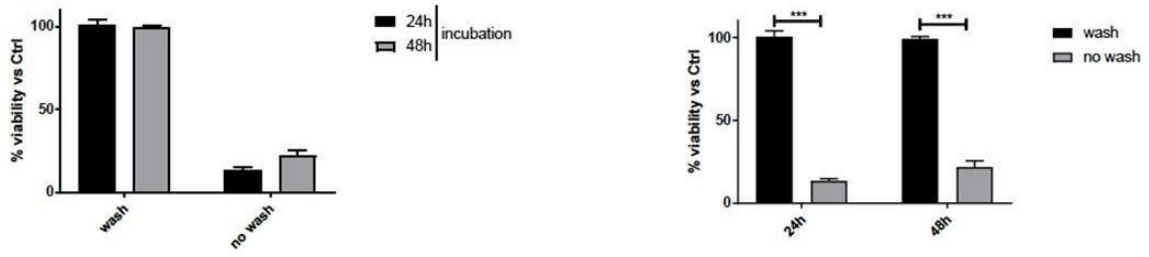

Fig. 3: Viability evaluation in U87-MG cells incubated for 24h and 48h with 100 µM DL-Ker-AuBPs and, on the right, illuminated for 6 minutes. Each evaluation was conducted after washing and not washing the excess of nanoparticles.

At the transmission electron microscope (TEM), DL-Ker-AuBPys were not aggregated but independent. Keratin coating was homogeneously present on the surface of the nanoparticles and in U87-MG cells after 24 and 48 hours of incubation, as illustrated in Figure 4.

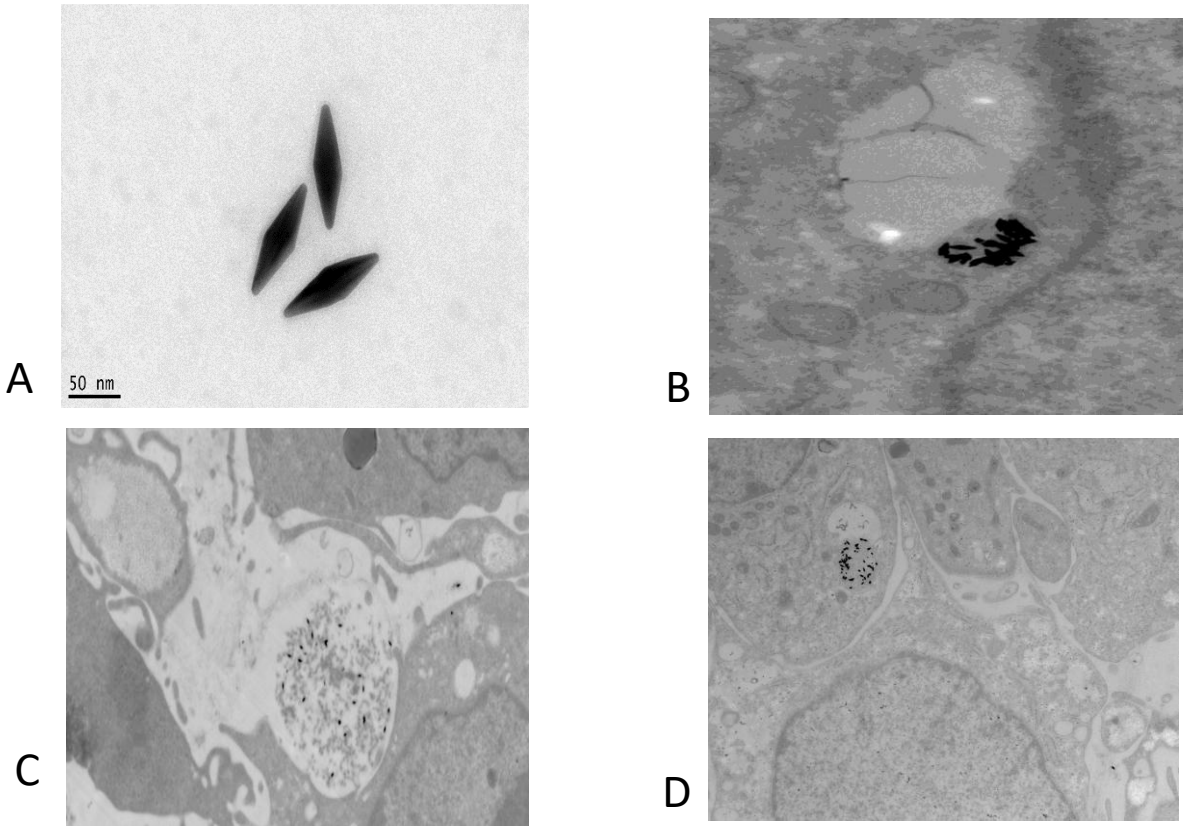

Fig. 4: in A, TEM image of the DL-Ker-AuBPys shows independent particles, no aggregation, and homogenous keratin coating on the nanoparticles' surface; in B, agglomerates of nanoparticles undergo cellular uptake; in C, DL-Ker-BPys are present inside the U87-MG cells after a 24-hour incubation; in D, DL-Ker-BPys are present inside the U87-MG cells after 48-hour incubation.

3.2 ITLC results with $^{223}RaCl_2$-DL-Ker-AuBPys

As a control experiment, to understand the behaviour in the two different mobile phases, a drop (5 µl) of $^{223}RaCl_2$ has been deposited on the strip for the NaCl mobile phase and another on the strip for the MEK mobile phase. The isotope migrated only with the NaCl mobile phase (fig. 5).

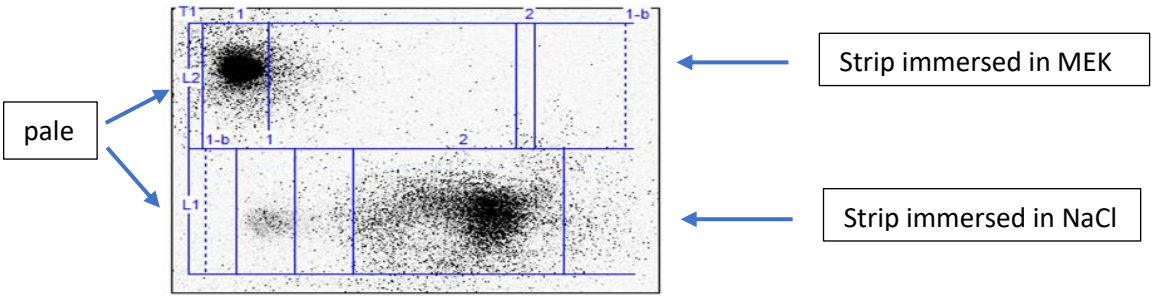

Fig. 5 Development of $^{223}RaCl_2$ in MEK and NaCl mobile phase. L1 is the strip immersed in NaCl, L2 the strip immersed in MEK. The darker area in cell 2 of L1 represents the migrated $^{223}RaCl_2$.

Then, 2 µl of $^{223}RaCl_2$ in 5 µl of DL-Ker-AuBPys at room temperature for 5, 15, and 30 minutes, then ITLC has been performed. The nanoparticles were labelled, but a part of the radium is unbound, as can be seen from the migration to the front of the strip immersed in physiological solution (fig. 6). No significant changes were observed in the label efficiency of DL-Ker-AuBPys when changing the incubation time.

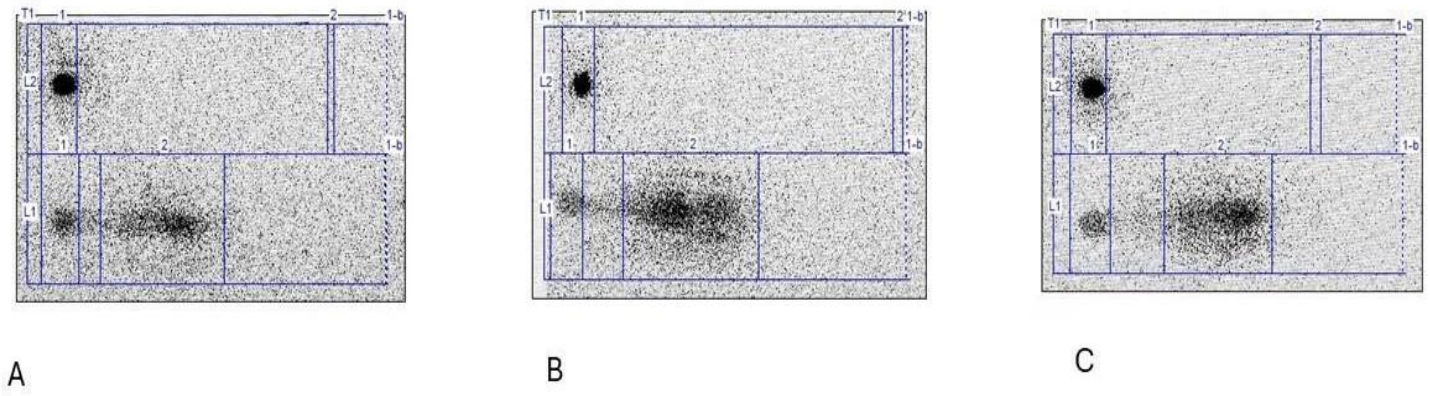

Fig. 6: ITLC results for DL-Ker-AuBPys labelled with 223RaCl2 through 5 minutes (A), 15 minutes (B), and 30 minutes (C) of incubation at room temperature. For each image, L1 represents the strip immersed in NaCl, and L2 the strip dipped in MEK. A part of the radioisotope was unbound, as seen in the back area in cell 2 of L1 in each ITLC result, showing that no better labelling was obtained by changing the incubation time.

The solution of DL-Ker-AuBPys and $^{223}RaCl_2$ was then heated to evaluate if the radiolabelling efficiency would have been improved. A total quantity of 0.5ml DL-Ker-AuBPys was placed vertically in a shielded water bath at 45°C and 0.25 ml of $^{223}RaCl_2$

was added. Samples were taken at 0, 5, 15, 30 minutes, and after 20 minutes of cooling at room temperature, ITLC was performed for each sample (fig. 7).

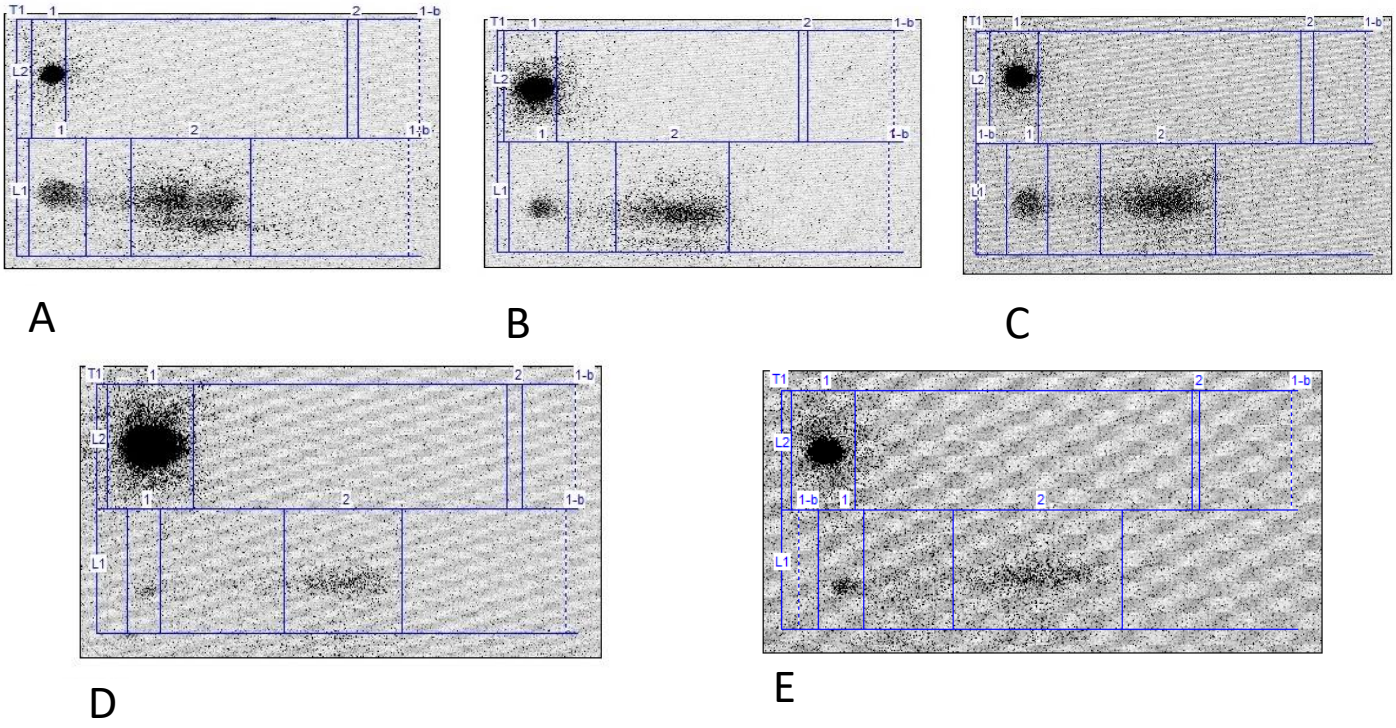

Fig. 7: ITLC for a sample taken from the $^{223}RaCl_2$-DL-Ker-AuBPys solution at time 0 (A), at 5 minutes (B), at 15 minutes (C), at 30 minutes (D) after warming at 45°C and after 20 minutes of cooling at room temperature after 30 minutes of warming at 45°C (E). For each image, L1 is the strip immersed in NaCl, and L2 the strip immersed in MEK. A part of the radioisotope remained unbound, as seen in the back area in cell 2 of L1 in each ITLC result.

3.3 pH results

The pH value was measured with a litmus test for the solution incubated at room temperature for 30 minutes and for the $^{223}RaCl_2$-DL-Ker-AuBPys solution at 20 minutes of cooling at room temperature after 30 minutes of warming at 45°C. In both cases, the pH value was 6 (fig. 8).

Fig. 8: pH value evaluation conducted with a litmus test for $^{223}RaCl_2$-DL-Ker-AuBPys incubated at room temperature for 30 minutes (A) and at 20 minutes of cooling at room temperature after 30 minutes of warming at 45°C (B). The pH value was assessed at 6. A significant change in pH value within the sensitivity limits of the measuring instrument could not be seen.

3.4 Reflectance spectra of the strips and absorbance spectra of nanoparticle solutions

Reflectance spectra were acquired for strips on which a drop of the $^{223}RaCl_2$-DL-Ker-AuBPys solution was deposited, respectively, after an incubation at room temperature for different times. In figure 9, a blue-shift of the longitudinal plasmon of the AuBPys is observed as the incubation time increases ($\Delta\lambda$=17nm). This, in accordance with the data acquired at the cyclone, suggests that the labelling of DL-Ker-AuBPys was successful.

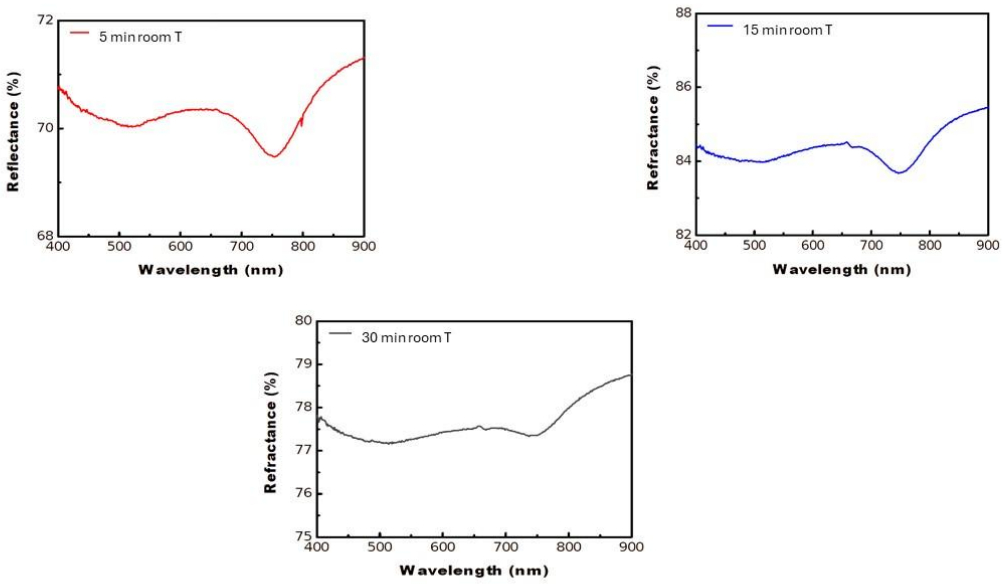

Fig. 9: Reflectance spectra of the ITLC strips containing a drop of $^{223}RaCl_2$-DL-Ker-AuBPs solutions with different times of incubation immersed in saline. The modification of the curves suggested effective radiolabelling.

Analogously, reflectance spectra were acquired for the strips with $^{223}RaCl_2$-DL-Ker-AuBPys solutions heated at 45° and taken up at time 0, 5, 15, 30 minutes, and 20 minutes after cooling at room temperature after 30 minutes of incubation (fig. 10). For short incubation times at 45°C (0, 10 minutes) a trend similar to incubation at room temperature is observed. After 15 min of incubation the longitudinal plasmon peak of AuBPys undergoes a red shift. From 15 minutes of incubation onwards the intensity of the peak progressively decreases, the spectra are noisy and difficult to interpret.

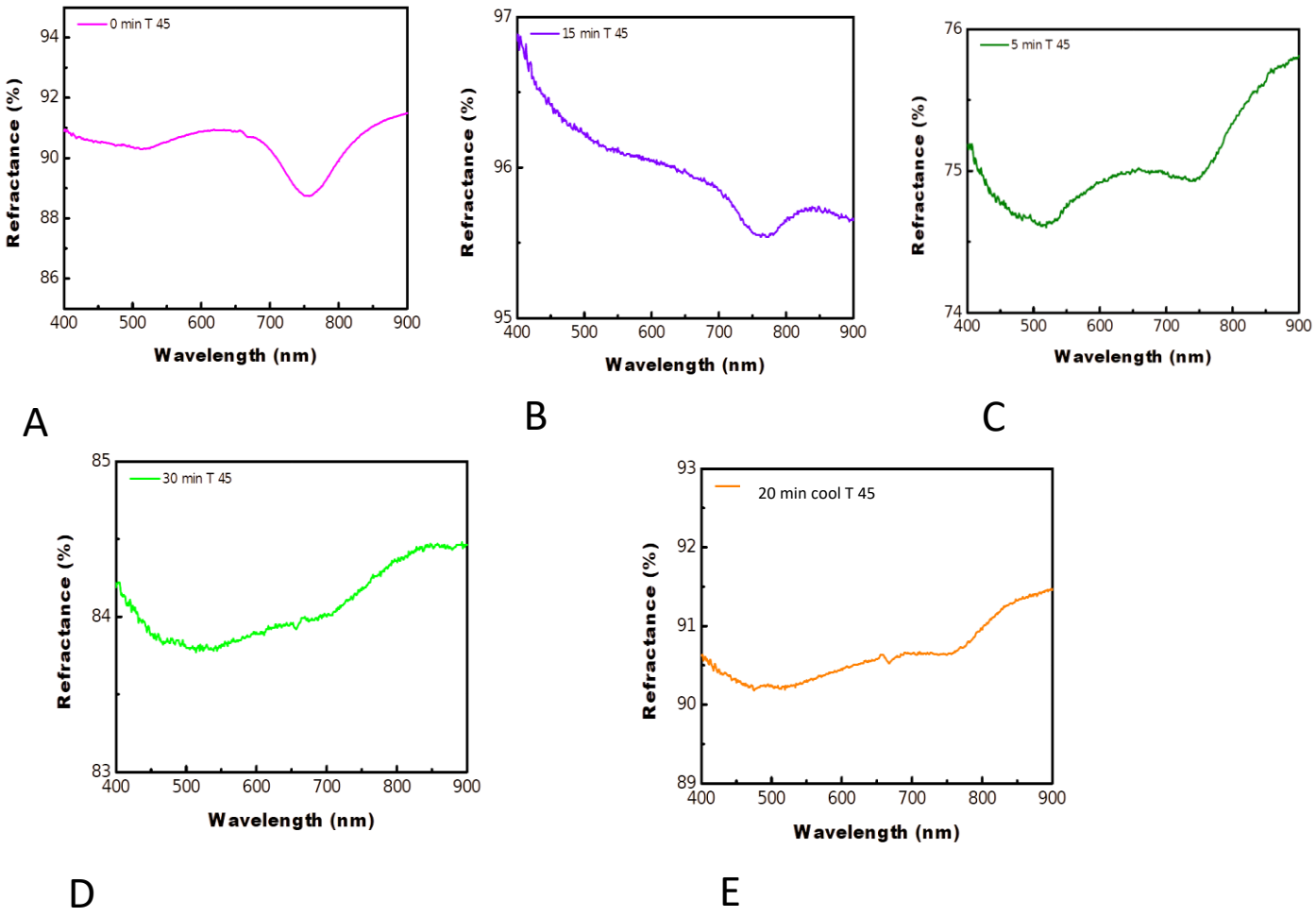

Fig. 10: reflectance spectra of the strips with the samples taken at different times from the solution of DL-Ker-AuBPys and $^{223}RaCl_2$ heated at 45°C. In A, at time 0 at 45°C; in B, 15 minutes of incubation at 45°C; in C, 5 minutes of incubation at 45°C; in D, 30 minutes of incubation at 45°C and in E, the same solution of figure D after 20 minutes of cooling.

Absorbance spectra were acquired for the solutions containing DL-Ker-AuBPys alone, $^{223}RaCl_2$-DL-Ker-AuBPys incubated at room temperature and heated.

From the analysis of the absorption spectra of the Ra and AuBPys solutions (fig. 11) a red-shift of the absorption peak associated with the longitudinal plasmon of the AuBPys can be observed. In particular, in the solution incubated at room temperature, there is a variation of $\Delta\lambda$=11 nm, and in the solution incubated at 45°C $\Delta\lambda$=16 nm. The peak intensity associated with the longitudinal plasmon of the AuBPys incubated at 45°C is significantly lower than that of the other two peaks.

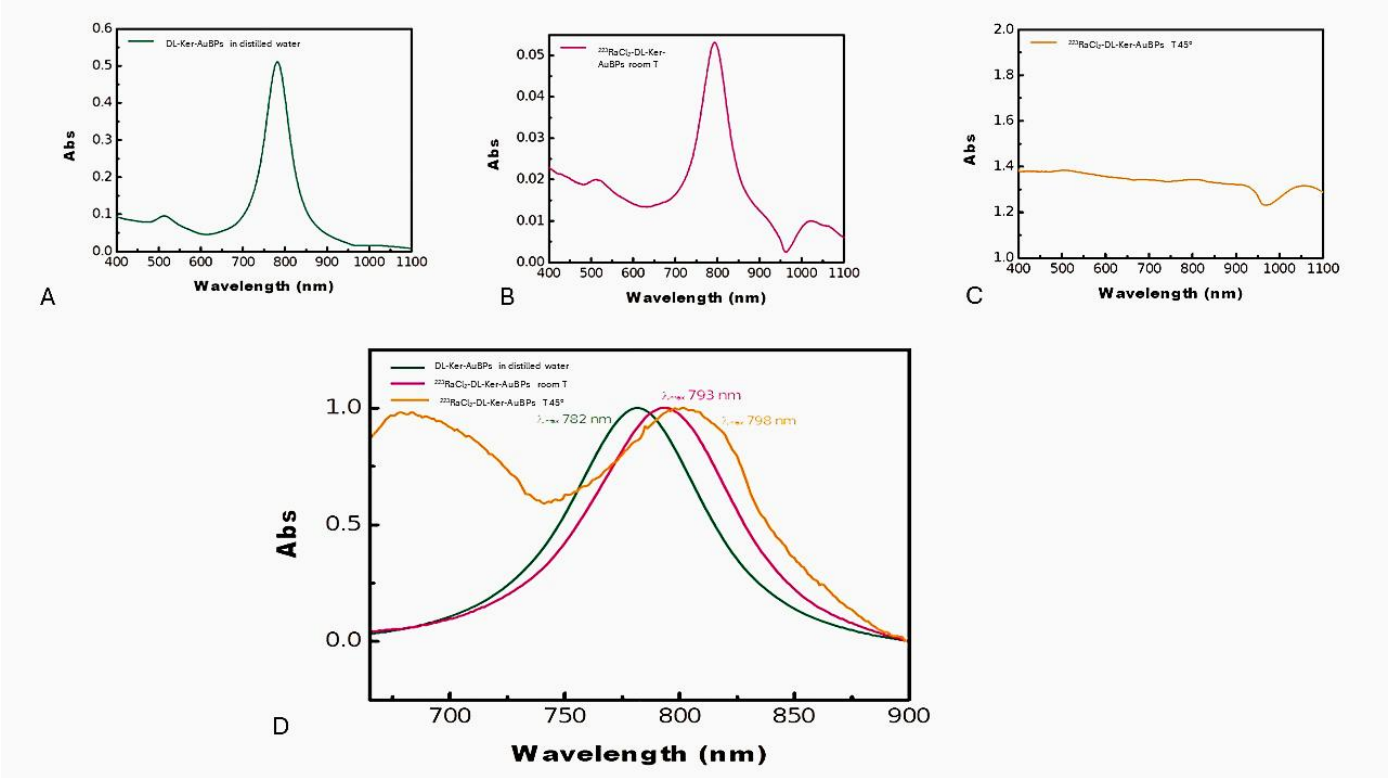

Fig. 11: absorbance spectra of nanoparticles in distilled water (A), $^{223}RaCl_2$-DL-Ker-AuBPys after the incubation at room temperature (B), after heating at 45°C(C), and the comparison between all the curves (D). The shift of the pink curve demonstrated effective labelling even if the nanoparticles seemed not to be stable after 45°C of warming as seen by the altered morphology of the yellow curve.

3.5 Thermal scan of the strips with $^{223}RaCl_2$-DL-Ker-AuBPys and DL-Ker-AuBPys

The strips described in section 3.2 were analyzed with the thermo-optical setup shown in section 2.8. The strips on which a drop of DL-Ker-AuBPys solution was deposited were compared with those on which a drop of $^{223}RaCl_2$-DL-Ker-AuBPys was deposited. Both samples were illuminated at steps of 3 mm from the point of solution deposition (fig. 12).

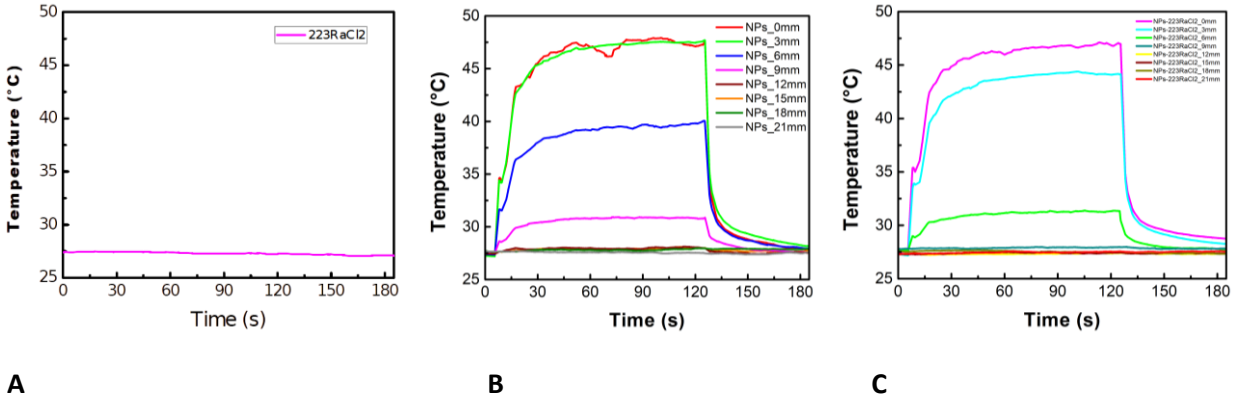

Fig. 12: thermal scans of the strip with a drop of $^{223}RaCl_2$ (A), with the DL-Ker-AuBPy alone (B), and with a drop of $^{223}RaCl_2$-DL-Ker-AuBPys solution (C).

The thermal profiles (fig. 13) reveal that in both samples, the most significant temperature increase occurs within 3mm of the solution deposition, confirming that nanoparticles do not migrate when deposited. The maximum temperatures reached by the two samples are comparable (Tmax(AuBPys)=47.6°C, Tmax (AuBPys+$RaCl_2$)=47.1°C). Both samples follow a logistic trend.

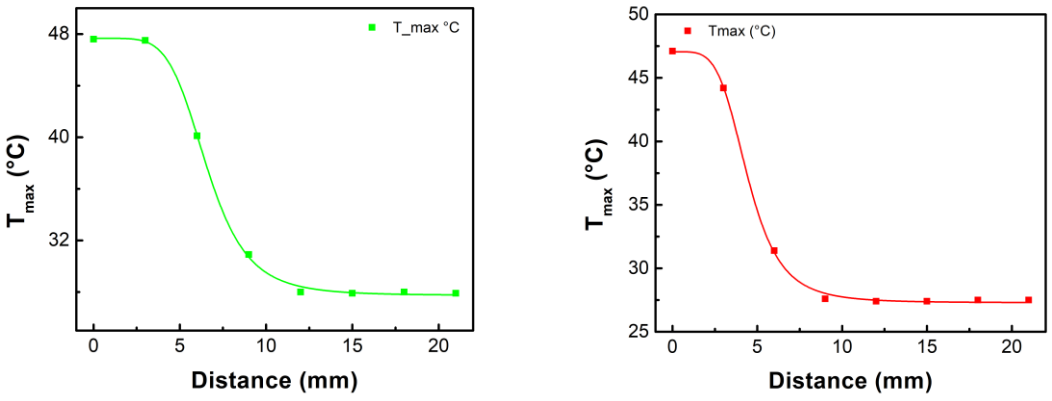

Fig. 13: Maximum temperature in function of the distance of pale in the strips containing DL-Ker-AuBPys drop (A) and $^{223}RaCl_2$-DL-Ker-AuBPys drop (B). The temperature is higher in proximity to the pale, suggesting this is the point at which the nanoparticles stay without migrating.

3.6 Gamma camera imaging

An equipped low-energy high-resolution collimator gamma camera was used to image the tube with DL-Ker-AuBPys and $^{223}RaCl_2$, which was incubated at room temperature for 5 minutes (Fig. 14).

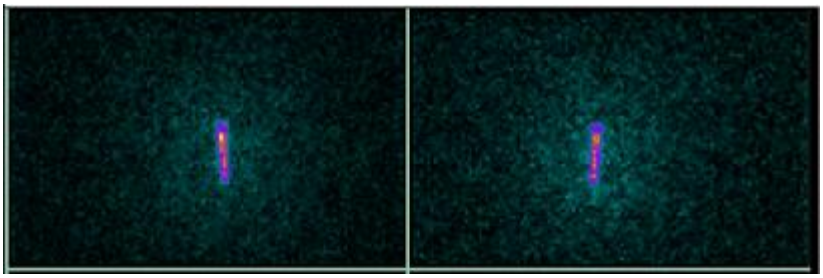

A B

Fig. 14: Gamma camera acquisition of the tube with DL-Ker-AuBPys and $^{223}RaCl_2$ incubated at room temperature for 5 minutes. A, anterior view; B, posterior view.

3.7 Evaluation of PTT effect

DL-Ker-AuBPys were tested for their photothermal capacity to induce cell death. U87-MG cells were incubated for 24 and 48 h with 100 µM of DL-Ker-AuBPys and illuminated for 6 minutes. Their viability was then evaluated. The results clearly showed the great photothermal capacity of DL-Ker-AuBPy that greatly induces cell death in U87-MG cells when they are not washed out before illumination. Contrarily, when the excess of nanoparticles is removed, they are not able to elevate the intracellular temperature enough to cause cell death, which could be due to a difficulty to penetrate the cell membrane caused by their size (fig. 15).

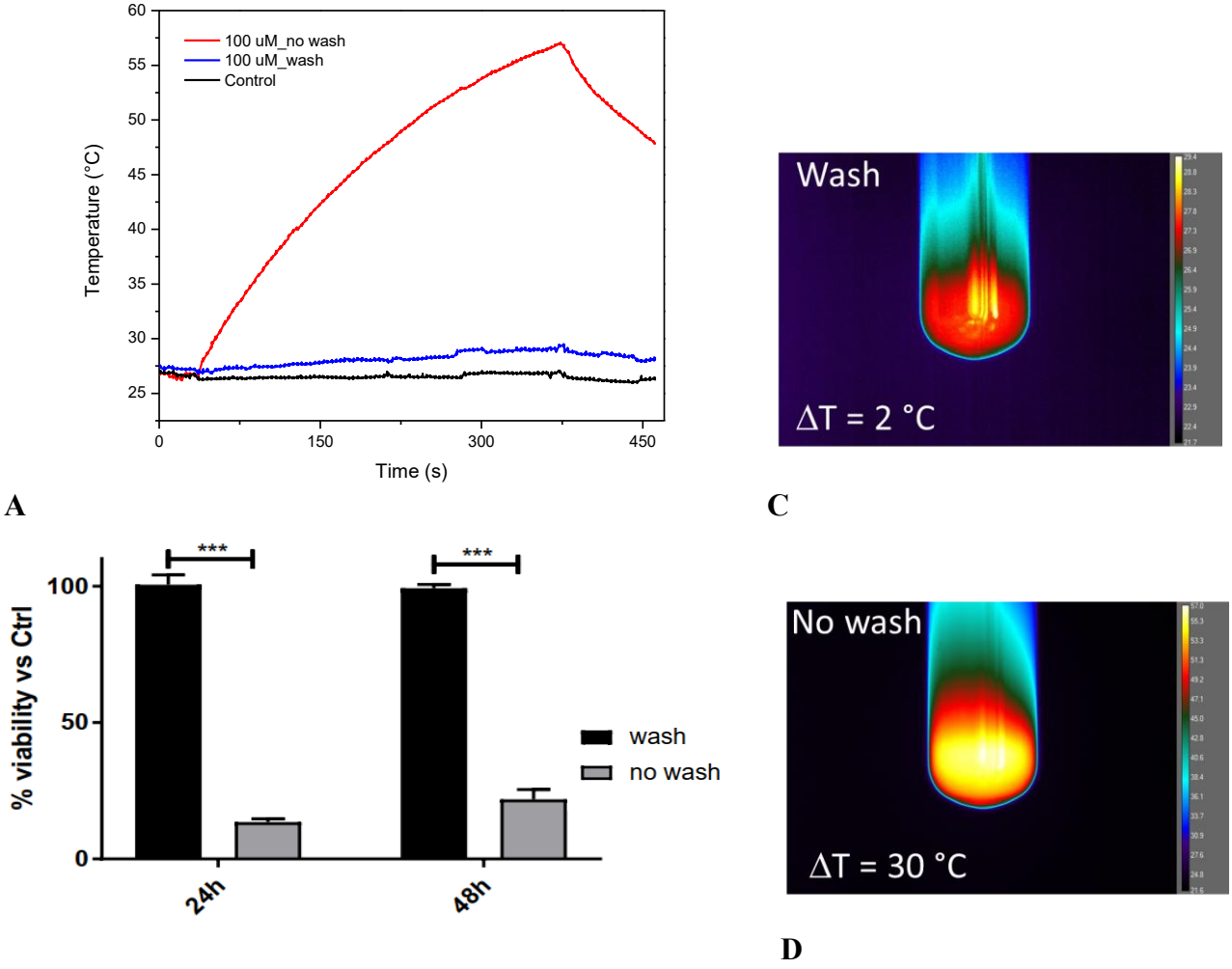

Fig.15: in A, the peak of the red curve indicating the increase of intracellular temperature of U87-MG cells incubated with 100 µM of DL-Ker-AuBPys after the illumination process without removing the excess of nanoparticles, while the blue curve represents the same situation when the excess is removed; in B viability (expressed as percentage vs control) of U87-MG cells incubated with Ker-AuBPys after the illumination process (represented by the strings with the 3 stars above on the bars). When the excess of nanoparticles is removed, C) the temperature in the cells increases only of 2°C, D) when the excess is not removed the temperature increases of about 30 °C, causing cellular death.

3.8 Absorbance spectrum of $^{223}RaCl_2$-gelatine-Na_2HPO_4-AuNRs

The absorbance spectrum of the original solution of AuNRs had an absorbance peak at 780 nm, while after the coating with gelatine the peak was 787 nm demonstrating the successful functionalization of nanorods. After 24 hours, the gelatine-AuNRs solution peak was at 793 nm and no sign of aggregation was visible in the spectrum (figures 16-17).

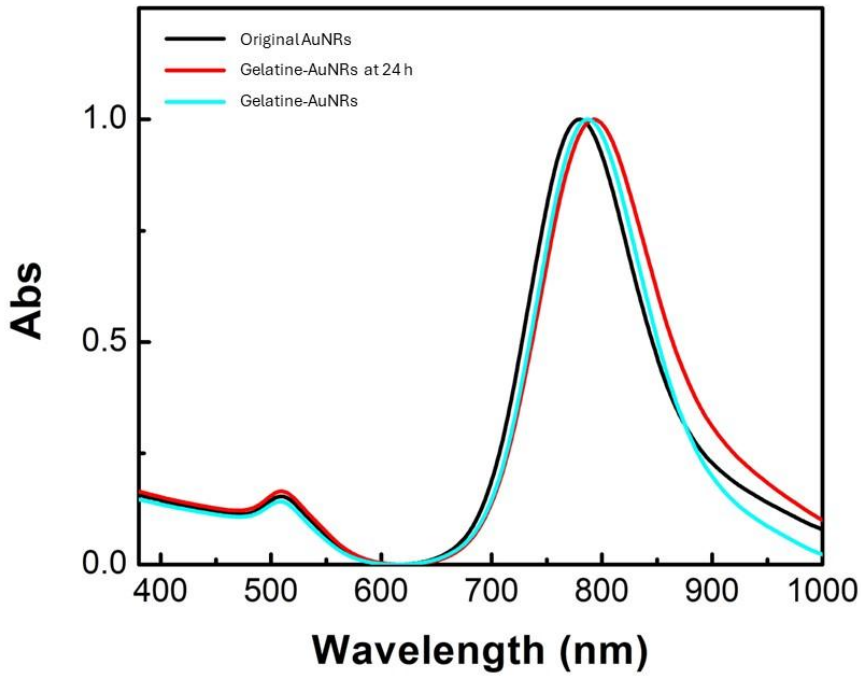

Fig. 16: absorbance spectra of original AuNRs solution, gelatine-AuNRs solution and gelatine-AuNRs after 24 hours. After 24 hour the gelatine-AuNRs were quite stable.

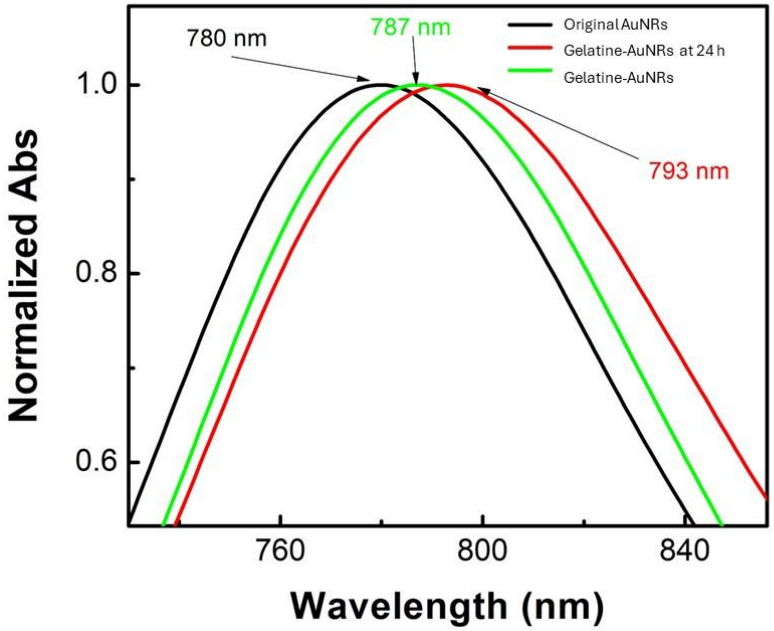

Fig. 17: comparison between the absorbance peak of the original AuNRs solution, gelatine-AuNRs and gelatine-AuNRs after 24 hours.

The spectra acquired after adding a total of 240 µL of decayed $^{223}RaCl_2$ to gelatine-Na_2HPO_4-AuNRs solution confirmed the effective binding with decayed $^{223}RaCl_2$: the slight right shift of the absorbance curve suggested the modification of the microenvironment around the nanorods (figures 18-19).

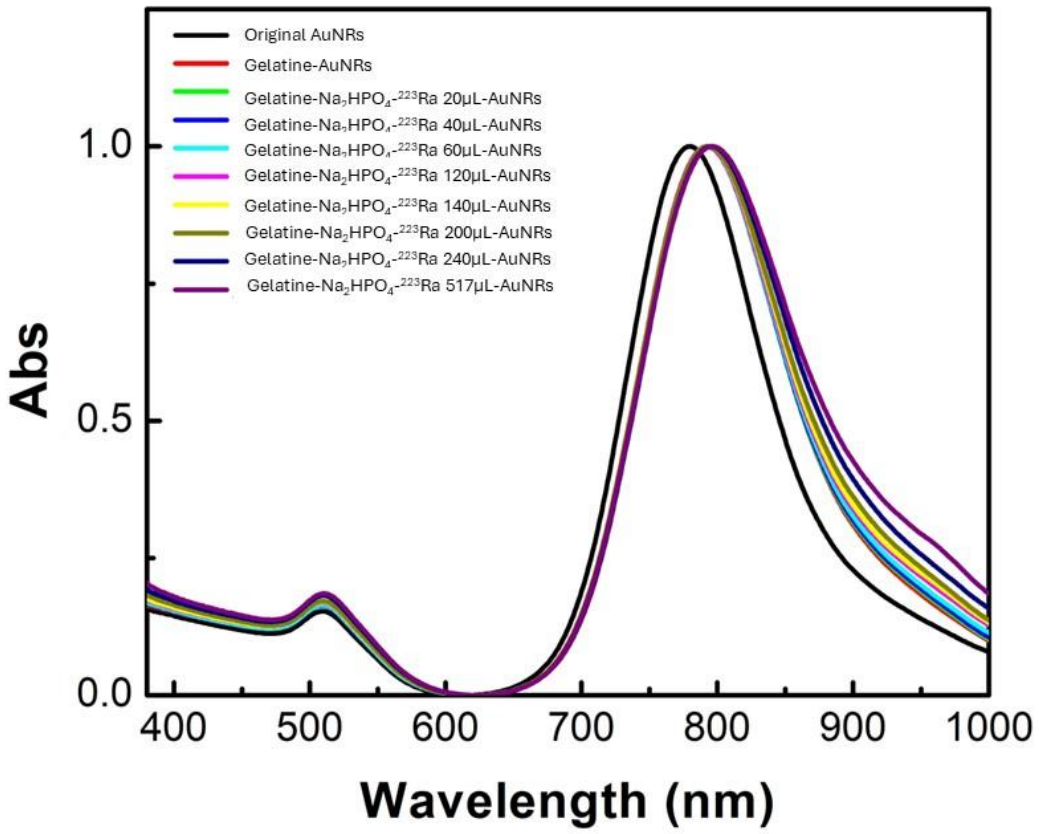

Fig. 18: absorbance curve of original solution of AuNRs, gelatine-AuRNs and $^{223}RaCl_2$-gelatine-Na_2HPO_4-AuNRs at different volume of $^{223}RaCl_2$ added.

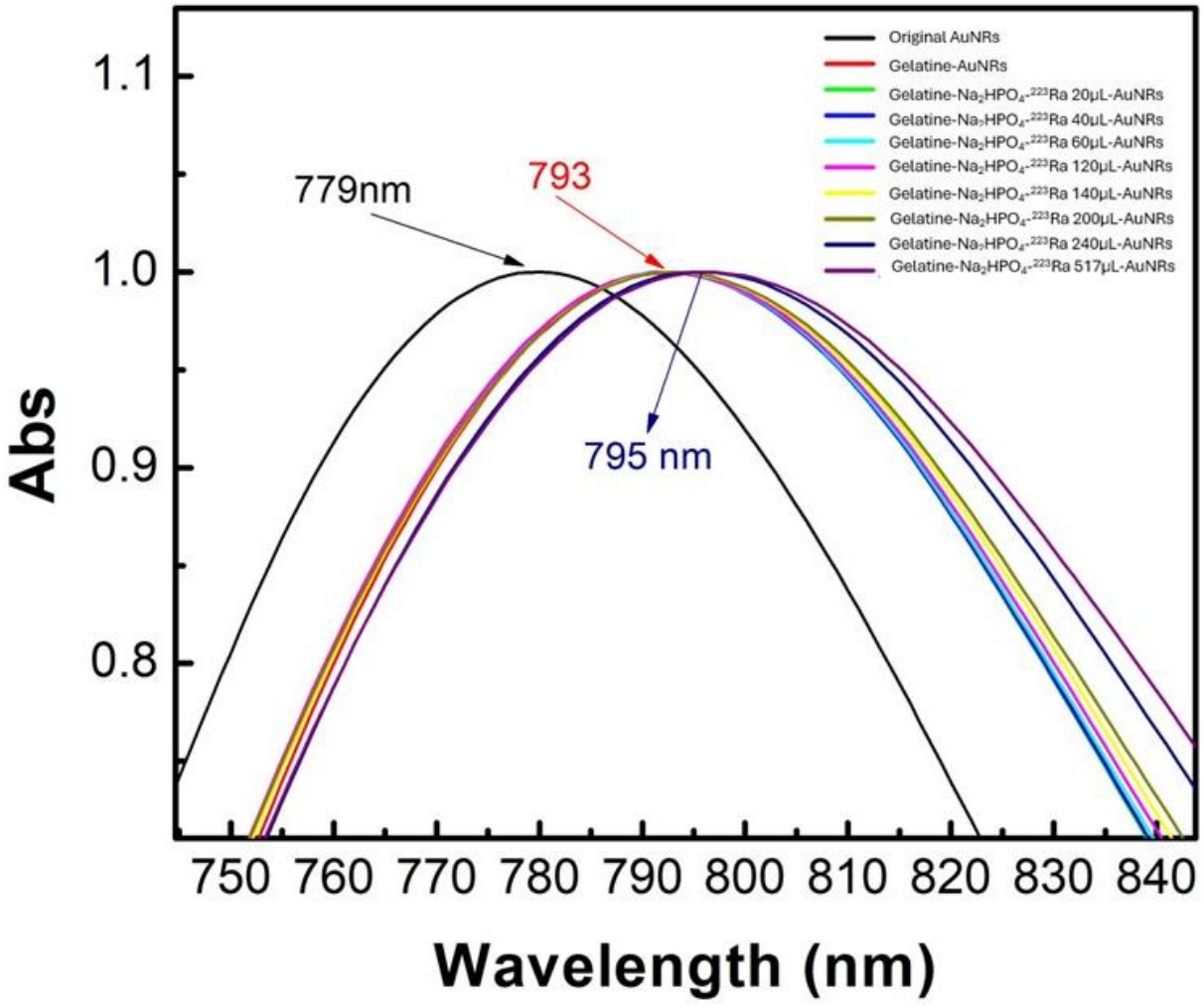

Fig. 19: absorbance peak of original solution of AuNRs (779 nm), gelatine-AuRNs (793 nm) and $^{223}RaCl_2$-gelatine-Na_2HPO_4-AuNRs at different volumes of $^{223}RaCl_2$ added. After the addition of 240 µL of decay $^{223}RaCl_2$, the right shift of the curve is visible (795 nm).

The nanoparticles began to aggregate when other 20 µL of decayed $^{223}RaCl_2$ (for a total of 517 µL) was added to gelatine-Na_2HPO_4 -AuNRs solution, as demonstrated by the presence of the right shoulder of the absorbance curve.

However, after 24 hours, the radiolabelled nanoparticles were stable as demonstrated by the comparison between the absorbance curve of gelatine-Na_2HPO_4-NRs labelled with 20 µL of decay $^{223}RaCl_2$ and the spectrum obtained after 24 hours of gelatine-Na_2HPO_4-NRs labelled with 517 µL of decay $^{223}RaCl_2$. The two spectra are similar (fig. 20-21).

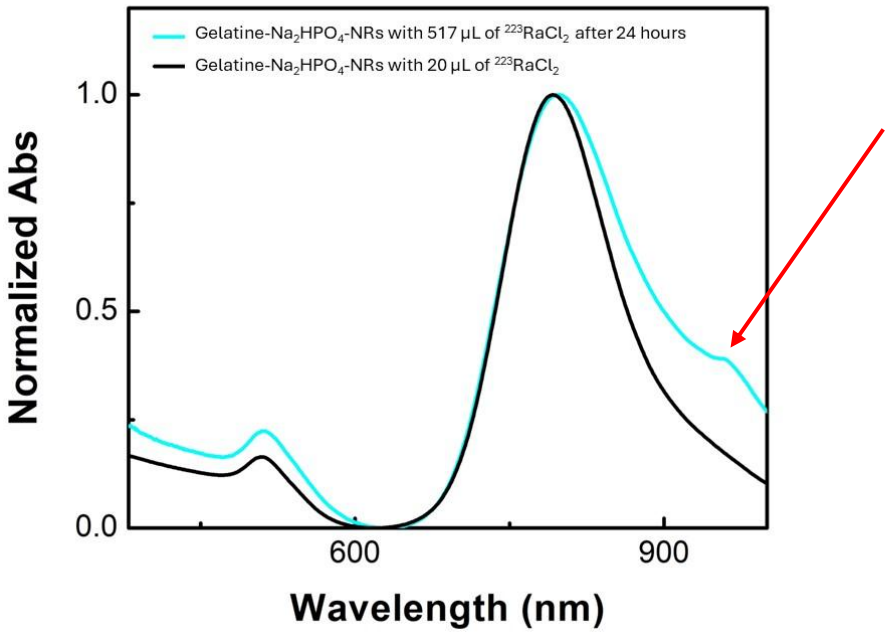

Fig. 20: absorbance spectra of gelatine-Na_2HPO_4-NRs labelled with 20 µL of decay $^{223}RaCl_2$ and the gelatine-Na_2HPO_4-NRs labelled with 517 µL of decay $^{223}RaCl_2$ after 24 hours. The right shoulder (indicated by the red arrow) visible in the curve obtained after 24 hours demonstrated the aggregation of nanoparticles.

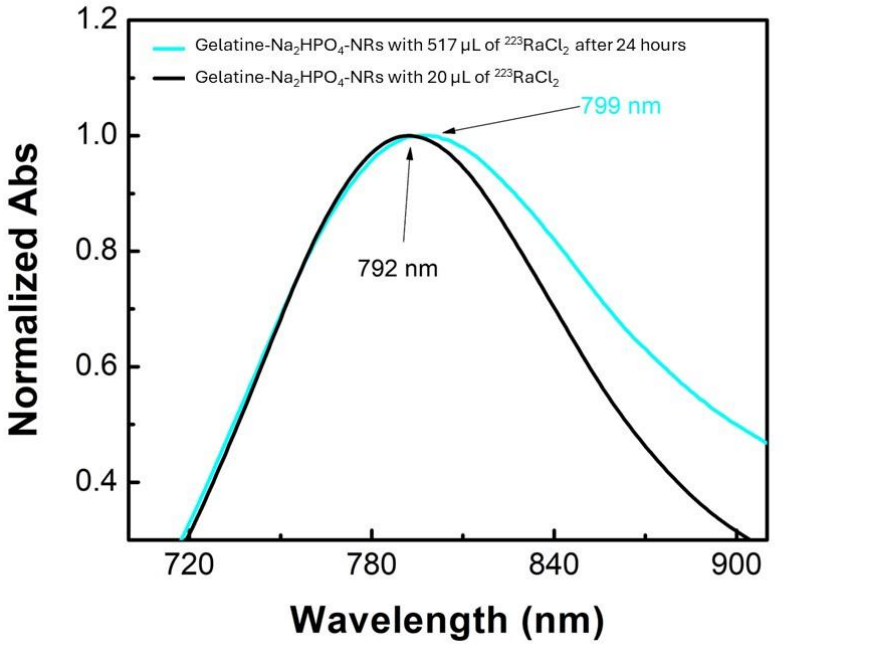

Fig. 21: comparison between the absorbance peak of gelatine-Na_2HPO_4-NRs labelled with 20 µL of decay $^{223}RaCl_2$ and the gelatine-Na_2HPO_4-NRs labelled with 517 µL of decay $^{223}RaCl_2$ after 24 hours.

3.9 Absorbance spectrum of AuNRs/PAH/Ab

The functionalization of the AuNRs with mouse monoclonal antibodies 1011:sc-57709 was successfully demonstrated by the absorbance spectra of AuNRs and AuNRs/PAH/Ab solution. The absorption spectrum of the AuNRs/PAH/Ab pointed to a shift of about 14 nm with respect to the AuNRs absorbance peak of 660 nm (fig. 22).

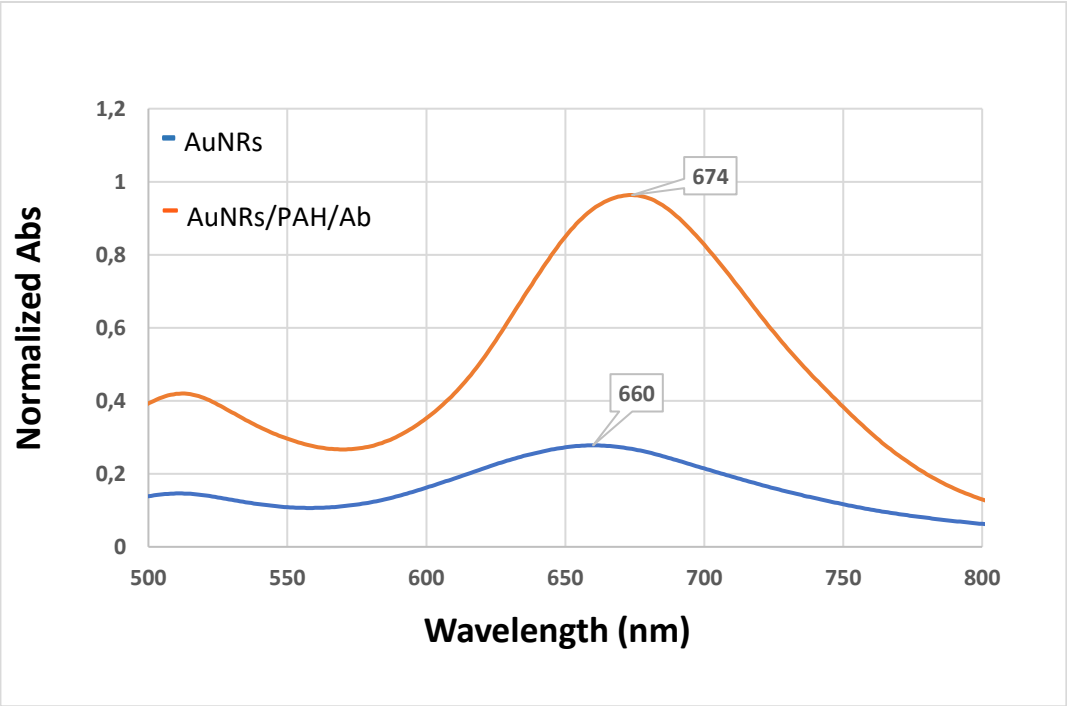

Fig. 22: comparison between the absorbance peak of AuNRs (blue curve) and AuNRs/PAH/Ab (orange curve). A slight shift of 14 nm is evident for AuNRs/PAH/Ab absorbance peak.

3.10 ITLC results with $^{223}RaCl_2$-DTPA-NRs

In the second part of the experiment, 0.5 ml of NRs was heated to 45 °C for 15 min, and 1 ml of DTPA was added. The incubation time with DTPA was 15 minutes.

After, 1 ml of Radium-223 was added to the solution. ITLC was performed after an incubation time with $^{223}RaCl_2$ of 10, 20, and 30 minutes.

In all the experiments, an excellent label efficacy was obtained, demonstrating the importance of the use of a chelator agent for the labelling of the AuNRs (fig. 23-25).

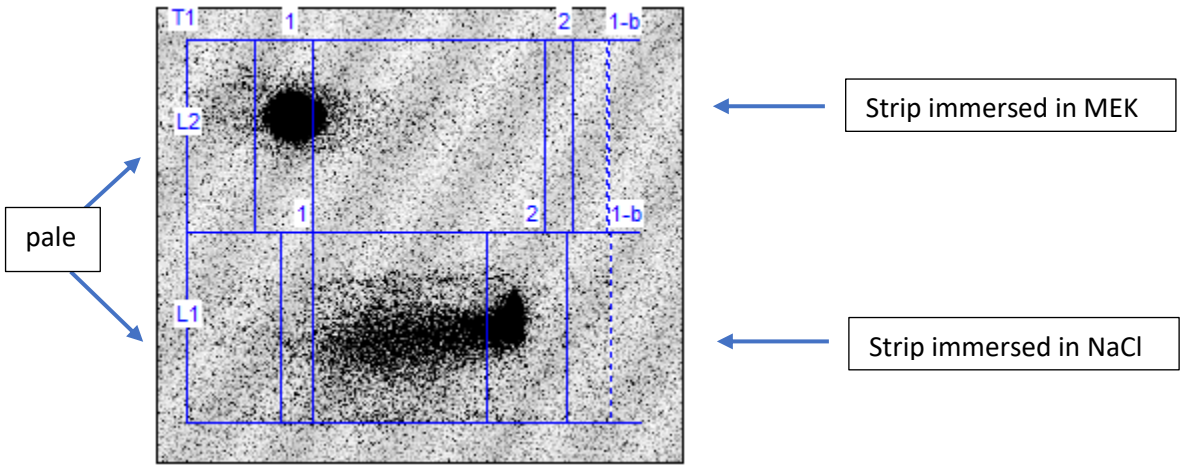

Fig. 23: Development of $^{223}RaCl_2$-DTPA-NRs in MEK and NaCl mobile phase after an incubation time with $^{223}RaCl_2$ of 10 minutes. L1 is the strip immersed in MEK, and L2 is the strip dipped in NaCl. The darker area in cell 2 of L1 represents the migrated $^{223}RaCl_2$-DTPA-NRs.

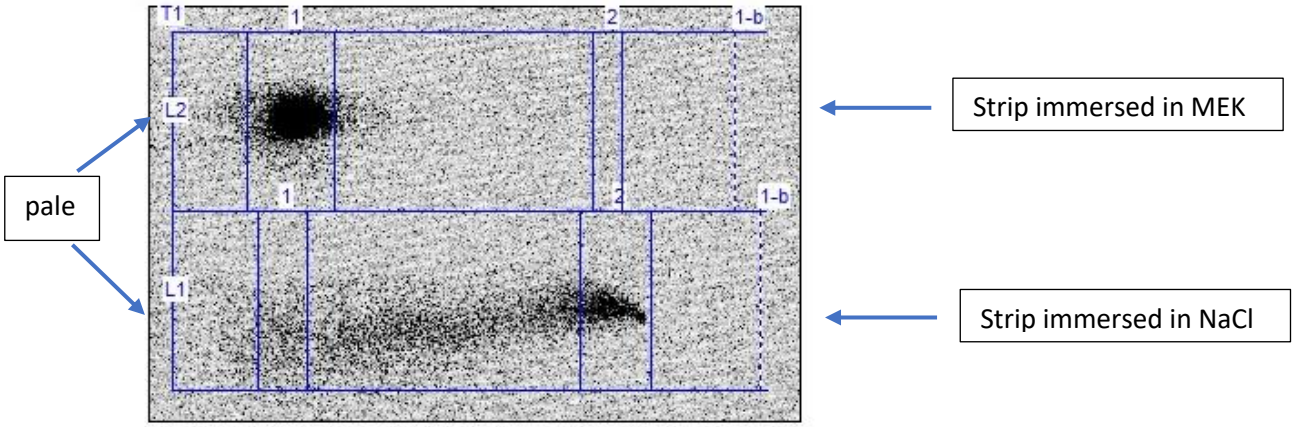

Fig. 24: Development of $^{223}RaCl_2$-DTPA-NRs in MEK and NaCl mobile phase after an incubation time with $^{223}RaCl_2$ of 20 minutes. L1 is the strip immersed in MEK, and L2 is the strip dipped in NaCl. The darker area in cell 2 of L1 represents the migrated $^{223}RaCl_2$-DTPA-NRs.

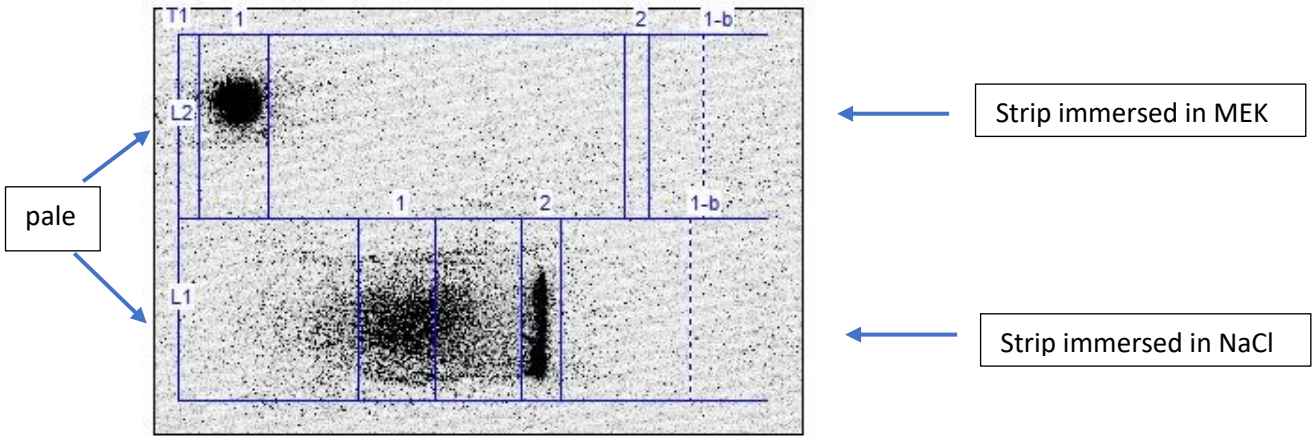

Fig. 25: Development of $^{223}RaCl_2$-DTPA-NRs in MEK and NaCl mobile phase after an incubation time with $^{223}RaCl_2$ of 30 minutes. L1 is the strip immersed in MEK, L2 is the strip immersed in NaCl. The darker area in cell 2 of L1 represents the migrated $^{223}RaCl_2$-DTPA-NRs.

4. Conclusions

Keratin functionalization was proposed to overcome the toxicity of CTAB used for the AuBP synthesis. DL-Ker-AuBPys demonstrated higher biocompatibility in viability assays with U87-MG. After laser irradiation, DL-Ker-AuBPys demonstrated excellent photothermal capacity compared to SL-Ker-AuBPs. Regarding radiolabelling, the first experiment performed by incubating the $^{223}RaCl_2$ with DL-Ker-AuBPys at room temperature for 5 min showed a labelling yield, evaluated by radiochromatography, equal to 7.8%. This percentage is encouraging but not sufficient for clinical trials. Therefore, in subsequent experiments, an attempt was made to increase the labelling yield by varying incubation time and temperature. For experiments at room temperature, DL-Ker-AuBPys were incubated for 5, 15, and 30 minutes. For experiments at 45 ºC, the incubation times were 0, 5, 15, and 30 minutes. A further experiment was carried out after 20 minutes of cooling at room temperature. No significant changes in the labelling yield or solutions' pH value were found. This means that it is not enough to increase incubation time and temperature to ameliorate the radiolabelling of DL-Ker-AuBPys with $^{223}RaCl_2$.

A possible hypothesis to explain low labelling yield is the presence of recoil energy produced by the decay of $^{223}RaCl_2$ that can prevent the establishment of a stable bond between the isotope and nanoparticles.

Subsequently, gelatine-Na_2HPO_4 was studied as possible chelating agent of NRs which were successfully labelled with 240 µL of decay $^{223}RaCl2$. However, when the total volume of added radium reached 517 µL, the nanoparticles aggregated. After 24 hours, AuNRs remained stable, even though initial signs of aggregation were observed in the absorbance spectrum.

However, there are two main limitations of this part of the study:

1. The absorbance spectrum of gelatine-Na_2HPO_4-NRs was not acquired for laboratory concerns. It is necessary to study the possible modification of the microenvironment around the nanoparticles to understand the potential role of Na_2HPO_4 for the radiolabelling.

2. During this experiment, only decay $^{223}RaCl_2$ was used for delivery issues, and maybe it could be in the form of ^{207}Pb. Since they have different atomic diameters and so different chemical profiles, it is necessary to employ not decayed radium for a more correct evaluation of the AuNRs labelling.

The absorbance peak of gelatine-AuNRs solution after 24 hours was 793 nm, while the peak of gelatine-AuNRs at time 0 was 787 nm, showing how 24 hours were necessary to better functionalize the AuNRs. Moreover, in this experiment, the superior limit of decayed radium allowed to be added before the aggregation of gelatine-Na_2HPO_4-AuNRs was 240 µL.

After the functionalization of AuNRs with DTPA, no residual activity was detected in the pale of the ITLC strips immersed in NaCl. This result was evident yet after 10 minutes of incubation with radium, assessing DTPA as a good chelating agent for the radiolabelling of AuNRs.

Moreover, an effective antibody labelling was seen when AuNRs were incubated with PAH/Ab. PAH surely mediates a good binding between the nanoparticle and the antibody.

AuNRs have been easily labelled through the use of the chelator agent, and their functionalization with the monoclonal antibody is feasible. Considering these findings, gold nanorods represent the perfect ally to produce a novel theragnostic instrument for the detection and treatment of NHL and paragranuloma micro metastases. However, further studies are required for clinical use.

References:

1. Frantellizzi, V.; Conte, M.; Pontico, M.; Pani, A.; Pani, R.; De Vincentis, G. New Frontiers in Molecular Imaging with Superparamagnetic Iron Oxide Nanoparticles (SPIONs): Efficacy, Toxicity, and Future Applications. *Nucl Med Mol Imaging* **2020**, *54*, 65–80, doi:10.1007/s13139-020-00635-w.

2. Sivakumar, B.; Aswathy, R.G.; Romero-Aburto, R.; Mitcham, T.; Mitchel, K.A.; Nagaoka, Y.; Bouchard, R.R.; Ajayan, P.M.; Maekawa, T.; Sakthikumar, D.N. Highly Versatile SPION Encapsulated PLGA Nanoparticles as Photothermal Ablators of Cancer Cells and as Multimodal Imaging Agents. *Biomater Sci* **2017**, *5*, 432–443, doi:10.1039/C6BM00621C.

3. *Active Plasmonic Nanomaterials*; De Sio, L., Ed.; Jenny Stanford Publishing, 2015; ISBN 9780429068416.

4. Frantellizzi, V.; Verrina, V.; Raso, C.; Pontico, M.; Petronella, F.; Bertana, V.; Ballesio, A.; Marasso, S.L.; Miglietta, S.; Rosa, P.; et al. 99mTc-Labeled Keratin Gold-Nanoparticles in a Nephron-like Microfluidic Chip for Photo-Thermal Therapy Applications. *Mater Today Adv* **2022**, *16*, 100286, doi:10.1016/j.mtadv.2022.100286.

5. Grosges, T.; Barchiesi, D. Gold Nanoparticles as a Photothermal Agent in Cancer Therapy: The Thermal Ablation Characteristic Length. *Molecules* **2018**, *23*, 1316, doi:10.3390/molecules23061316.

6. De Angelis, B.; Depalo, N.; Petronella, F.; Quintarelli, C.; Curri, M.L.; Pani, R.; Calogero, A.; Locatelli, F.; De Sio, L. Stimuli-Responsive Nanoparticle-Assisted Immunotherapy: A New Weapon against Solid Tumours. *J Mater Chem B* **2020**, *8*, 1823–1840, doi:10.1039/c9tb02246e.

7. Frantellizzi, V.; Cosma, L.; Brunotti, G.; Pani, A.; Spanu, A.; Nuvoli, S.; De Cristofaro, F.; Civitelli, L.; De Vincentis, G. Targeted Alpha Therapy with Thorium-227. *Cancer Biother Radiopharm* **2020**, *35*, 437–445, doi:10.1089/cbr.2019.3105.

8. Thandra, K.C.; Barsouk, A.; Saginala, K.; Padala, S.A.; Barsouk, A.; Rawla, P. Epidemiology of Non-Hodgkin's Lymphoma. *Medical Sciences* **2021**, *9*, 5, doi:10.3390/medsci9010005.

9. Read, E.D.; Eu, P.; Little, P.J.; Piva, T.J. The Status of Radioimmunotherapy in CD20+ Non-Hodgkin's Lymphoma. *Target Oncol* **2015**, *10*, 15–26, doi:10.1007/s11523-014-0324-y.

10. Willard, P.; McKay, J.; Yazbeck, V. Role of Antibody-Based Therapy in Indolent Non-Hodgkin's Lymphoma. *Leuk Res Rep* **2021**, *16*, 100275, doi:10.1016/j.lrr.2021.100275.

11. Tedder, T.F.; Boyd, A.W.; Freedman, A.S.; Nadler, L.M.; Schlossman, S.F. The B Cell Surface Molecule B1 Is Functionally Linked with B Cell Activation and Differentiation. *J Immunol* **1985**, *135*, 973–979.

12. Bubien, J.K.; Zhou, L.J.; Bell, P.D.; Frizzell, R.A.; Tedder, T.F. Transfection of the CD20 Cell Surface Molecule into Ectopic Cell Types Generates a Ca2+ Conductance Found Constitutively in B Lymphocytes. *Journal of Cell Biology* **1993**, *121*, 1121–1132, doi:10.1083/jcb.121.5.1121.

13. Saarinen, S.; Pukkala, E.; Vahteristo, P.; Mäkinen, M.J.; Franssila, K.; Aaltonen, L.A. High Familial Risk in Nodular Lymphocyte-Predominant Hodgkin Lymphoma. *Journal of Clinical Oncology* **2013**, *31*, 938–943, doi:10.1200/JCO.2012.43.5958.

14. Diehl, V.; Sextro, M.; Franklin, J.; Hansmann, M.-L.; Harris, N.; Jaffe, E.; Poppema, S.; Harris, M.; Franssila, K.; van Krieken, J.; et al. Clinical Presentation, Course, and Prognostic Factors in Lymphocyte-Predominant Hodgkin's Disease and Lymphocyte-Rich Classical Hodgkin's Disease: Report From the European Task Force on Lymphoma Project on Lymphocyte-Predominant Hodgkin's Disease. *Journal of Clinical Oncology* **1999**, *17*, 776–776, doi:10.1200/JCO.1999.17.3.776.

15. Hansmann, M.-L.; Stein, H.; Fellbaum, C.; Hui, P.K.; Parwaresch, M.R.; Lennert, K. Nodular Paragranuloma Can Transform into High-Grade Malignant Lymphoma of B Type. *Hum Pathol* **1989**, *20*, 1169–1175, doi:10.1016/S0046-8177(89)80007-3.

16. Anagnostopoulos, I.; Hansmann, M.L.; Franssila, K.; Harris, M.; Harris, N.L.; Jaffe, E.S.; Han, J.; van Krieken, J.M.; Poppema, S.; Marafioti, T.; et al. European Task Force on Lymphoma Project on Lymphocyte Predominance Hodgkin Disease: Histologic and Immunohistologic Analysis of Submitted Cases Reveals 2 Types of Hodgkin Disease with a Nodular Growth Pattern and Abundant Lymphocytes. *Blood* **2000**, *96*, 1889–1899.

17. Brune, V.; Tiacci, E.; Pfeil, I.; Döring, C.; Eckerle, S.; van Noesel, C.J.M.; Klapper, W.; Falini, B.; von Heydebreck, A.; Metzler, D.; et al. Origin and Pathogenesis of Nodular Lymphocyte–Predominant Hodgkin Lymphoma as Revealed by Global Gene Expression Analysis. *Journal of Experimental Medicine* **2008**, *205*, 2251–2268, doi:10.1084/jem.20080809.

18. Hartmann, S.; Schuhmacher, B.; Rausch, T.; Fuller, L.; Döring, C.; Weniger, M.; Lollies, A.; Weiser, C.; Thurner, L.; Rengstl, B.; et al. Highly Recurrent Mutations of SGK1, DUSP2 and JUNB in Nodular Lymphocyte Predominant Hodgkin Lymphoma. *Leukemia* **2016**, *30*, 844–853, doi:10.1038/leu.2015.328.

19. Ayala-Orozco, C.; Urban, C.; Bishnoi, S.; Urban, A.; Charron, H.; Mitchell, T.; Shea, M.; Nanda, S.; Schiff, R.; Halas, N.; et al. Sub-100nm Gold Nanomatryoshkas Improve Photo-Thermal Therapy Efficacy in Large and Highly Aggressive Triple Negative Breast Tumors. *Journal of Controlled Release* **2014**, *191*, 90–97, doi:10.1016/j.jconrel.2014.07.038.

20. Link, S.; El-Sayed, M.A. Shape and Size Dependence of Radiative, Non-Radiative and Photothermal Properties of Gold Nanocrystals. *Int Rev Phys Chem* **2000**, *19*, 409–453, doi:10.1080/01442350050034180.

21. Rosa, P.; Scibetta, S.; Pepe, G.; Mangino, G.; Capocci, L.; Moons, S.J.; Boltje, T.J.; Fazi, F.; Petrozza, V.; Di Pardo, A.; et al. Polysialic Acid Sustains the Hypoxia-Induced Migration and Undifferentiated State of Human Glioblastoma Cells. *Int J Mol Sci* **2022**, *23*, 9563, doi:10.3390/ijms23179563.

22. Scibetta, S.; Miceli, M.; Iuliano, M.; Stefanuto, L.; Carbone, E.; Piscopo, P.; Petrozza, V.; Romeo, G.; Mangino, G.; Calogero, A.; et al. In Vitro Evaluation of the Antioxidant Capacity of 3,3-Disubstituted-3H-Benzofuran-2-One Derivatives in a Cellular Model of Neurodegeneration. *Life* **2024**, *14*, 422, doi:10.3390/life14040422.

23. Campu, A.; Lerouge, F.; Chateau, D.; Chaput, F.; Baldeck, P.; Parola, S.; Maniu, D.; Craciun, A.M.; Vulpoi, A.; Astilean, S.; et al. Gold NanoBipyramids Performing as Highly Sensitive Dual-Modal Optical Immunosensors. *Anal Chem* **2018**, *90*, 8567–8575, doi:10.1021/acs.analchem.8b01689.

24. Kimling, J.; Maier, M.; Okenve, B.; Kotaidis, V.; Ballot, H.; Plech, A. Turkevich Method for Gold Nanoparticle Synthesis Revisited. *J Phys Chem B* **2006**, *110*, 15700–15707, doi:10.1021/jp061667w.

25. Guglielmelli, A.; Rosa, P.; Contardi, M.; Prato, M.; Mangino, G.; Miglietta, S.; Petrozza, V.; Pani, R.; Calogero, A.; Athanassiou, A.; et al. Biomimetic Keratin Gold Nanoparticle-Mediated *in Vitro* Photothermal Therapy on Glioblastoma Multiforme. *Nanomedicine* **2021**, *16*, 121–138, doi:10.2217/nnm-2020-0349.